

***Model for Simulation of Hydride  
Precipitation in Zr-Based Used  
Fuel Claddings: A Status Report  
on Current Model Capabilities***

**Fuel Cycle Research & Development**

*Prepared for  
U.S. Department of Energy  
Used Fuel Disposition Campaign  
Veena Tikare and Philippe F. Weck  
Sandia National Laboratories  
Michael V. Glazoff  
Idaho National Laboratory  
August 30, 2013  
FCRD-UFD-2013-000251  
SAND2013-7154P*



**DISCLAIMER**

This information was prepared as an account of work sponsored by an agency of the U.S. Government. Neither the U.S. Government nor any agency thereof, nor any of their employees, makes any warranty, expressed or implied, or assumes any legal liability or responsibility for the accuracy, completeness, or usefulness, of any information, apparatus, product, or process disclosed, or represents that its use would not infringe privately owned rights. References herein to any specific commercial product, process, or service by trade name, trade mark, manufacturer, or otherwise, does not necessarily constitute or imply its endorsement, recommendation, or favoring by the U.S. Government or any agency thereof. The views and opinions of authors expressed herein do not necessarily state or reflect those of the U.S. Government or any agency thereof.

UNCLASSIFIED UNLIMITED RELEASE



Sandia National Laboratories is a multi-program laboratory managed and operated by Sandia Corporation, a wholly owned subsidiary of Lockheed Martin Corporation, for the U.S. Department of Energy National Nuclear Security Administration under contract DE-AC04-94AL85000.

Revision 2  
 12/20/2012

**APPENDIX E**  
**FCT DOCUMENT COVER SHEET <sup>1</sup>**

Name/Title of Deliverable/Milestone/Revision No. Model for Simulation of Hydride Precipitation in Zr-Based Used Fuel Claddings, A Status Report on Current Model Capabilities

Work Package Title and Number \_\_\_\_\_

Work Package WBS Number FT-13SN081003

Responsible Work Package Manager Veena Tikare *Veena Tikare* \_\_\_\_\_  
 (Name/Signature)

Date Submitted \_\_\_\_\_

Quality Rigor Level for Deliverable/Milestone <sup>2</sup>	<input checked="" type="checkbox"/> QRL-3	<input type="checkbox"/> QRL-2	<input type="checkbox"/> QRL-1 Nuclear Data	<input type="checkbox"/> Lab/Participant QA Program (no additional FCT QA requirements)
--	---	--------------------------------	--	---

This deliverable was prepared in accordance with Sandia National Laboratories  
 (Participant/National Laboratory Name)

QA program which meets the requirements of  
 DOE Order 414.1     NQA-1-2000     Other

**This Deliverable was subjected to:**

- |   |  |
|---|--|
| <input checked="" type="checkbox"/> Technical Review                  | <input type="checkbox"/> Peer Review                       |
| <b>Technical Review (TR)</b>  | <b>Peer Review (PR)</b>                                    |
| <b>Review Documentation Provided</b>                                  | <b>Review Documentation Provided</b>                       |
| <input type="checkbox"/> Signed TR Report or,                         | <input type="checkbox"/> Signed PR Report or,              |
| <input type="checkbox"/> Signed TR Concurrence Sheet or,              | <input type="checkbox"/> Signed PR Concurrence Sheet or,   |
| <input checked="" type="checkbox"/> Signature of TR Reviewer(s) below | <input type="checkbox"/> Signature of PR Reviewer(s) below |

**Name and Signature of Reviewers**  
*[Signature]* K. CLARVO \_\_\_\_\_  
 \_\_\_\_\_  
 \_\_\_\_\_

**NOTE 1:** Appendix E should be filled out and submitted with the deliverable. Or, if the PICS:NE system permits, completely enter all applicable information in the PICS:NE Deliverable Form. The requirement is to ensure that all applicable information is entered either in the PICS:NE system or by using the FCT Document Cover Sheet.

**NOTE 2:** In some cases there may be a milestone where an item is being fabricated, maintenance is being performed on a facility, or a document is being issued through a formal document control process where it specifically calls out a formal review of the document. In these cases, documentation (e.g., inspection report, maintenance request, work planning package documentation or the documented review of the issued document through the document control process) of the completion of the activity, along with the Document Cover Sheet, is sufficient to demonstrate achieving the milestone. If QRL 1, 2, or 3 is not assigned, then the Lab / Participant QA Program (no additional FCT QA requirements) box must be checked, and the work is understood to be performed and any deliverable developed in conformance with the respective National Laboratory / Participant, DOE or NNSA-approved QA Program.



## **SUMMARY**

This report satisfies a level 2 milestone for the Used Fuel Campaign's (UFD's) Science and Technology, Engineering Analysis of Storage and Transportation Project. It demonstrates a meso-scale, microstructural evolution model for simulation of zirconium hydride precipitation in the cladding of used fuels during long-term dry-storage. While the Zr-based claddings are manufactured free of any hydrogen, they absorb hydrogen during service, in the reactor by a process commonly termed 'hydrogen pick-up'. The amount of hydrogen that the cladding picks up is primarily a function of the exact chemistry and microstructure of the claddings and reactor operating conditions such as time-temperature history, and irradiation conditions. The hydrogen in the cladding is known to have consequences for the engineering performance of the cladding both in reactor and during post-service used fuel storage. The structural engineering performance of the cladding during long-term dry storage is of interest to UFD.

One of the barriers available for containment of radioactive fission products and fuel is the Zr-based cladding. Ensuring the structural integrity of the cladding is of great importance and requires understanding all mechanisms that could degrade performance. The precipitation and growth of zirconium hydrides during dry-storage is one of the most likely fuel rod integrity failure mechanisms either by embrittlement or delayed hydride cracking of the cladding (Hanson et al., 2011). While the phenomenon is well documented and identified as a key failure mechanism during long-term dry-storage (Birk et al., 2012 and NUREG/CR-7116), the ability to actually predict the formation of hydrides is poor. The model being developed in this work is to develop computational capability for the prediction of hydride formation in a stockpile of claddings of used fuels.

The model being developed for predicting hydride formation is a recently developed hybrid Potts-phase field model that combines elements of Potts Monte Carlo and the phase-field model to treat coupled microstructural-compositional evolution. Both models as well as the hybrid are materials models that simulate the evolution of microstructure along physically realistic paths to minimize the total free energy of the materials system given kinetic parameters for the evolution. To achieve this, the starting microstructure of Zircaloy-4 and the thermodynamic properties along with an understanding of the hydride formation mechanisms are needed. In this report, the model along with the starting microstructure, thermodynamics of the Zr-H system and the hydride formation mechanism is described. A demonstration of the model on the Zircaloy-4 microstructure is presented.

This document demonstrates a basic hydride precipitation model. This hydride precipitation model is built on a recently developed model that is a hybrid of the Potts kinetic Monte Carlo and phase-field model (Homer et al., 2013; Tikare and Schultz, 2012). The capabilities incorporated are:

1. A realistic microstructure was generated for the Zircaloy-4 with both geometric and crystallographic texture. Based on findings in the literature, the capability of generating a rolled microstructure with elongated grains matching the aspect ratio of published data was demonstrated. Furthermore, the crystallographic grain orientations were assigned based on texture data also found in the published literature.
2. The free energies of the two pertinent phases,  $\alpha$ -Zr and  $\delta$ -ZrH<sub>1.5</sub>, were calculated and incorporated into the hydride model. CALPHAD-type thermodynamics calculations were used to generate free-energy data for the Zr-H system with four phases, i.e. the matrix  $\alpha$ -Zr and the three hydride phases  $\gamma$ -ZrH,  $\delta$ -ZrH<sub>1.5</sub>, and  $\epsilon$ -ZrH<sub>2</sub>. The free energies of the two pertinent phases,  $\alpha$ -Zr and  $\delta$ -ZrH<sub>1.5</sub>, were fitted to generate smooth free-energy curves and incorporated into the hydride model. Furthermore, the chemical potential that drives the compositional and phase changes were up-graded in the model to simulate more complex materials with more components and more phases, as necessary, for future simulations.

3. The hybrid Potts-phase field model was modified to include crystallographic texture so that hydride precipitate nucleation and growth would occur along particular crystallographic directions. The demonstration in this work assumes precipitates grow along particular crystallographic directions, as these directions are thermodynamically favored growth directions.
4. The model can distribute nucleation sites in the microstructure to match known nucleation behavior. Nucleation is thought to occur at defects, such as dislocation loops and near grain boundaries. These capabilities are demonstrated in the model by treating the case of nuclei distributed randomly with uniform probability of occurring anywhere in the grains and preferentially occurring near grain boundaries.
5. Hydride precipitate growth is simulated in stress-free claddings and in one with a constant, uniaxial stress applied to show that the hybrid model is capable of incorporating local micro-mechanical stress state. The local stress state, due to the pressure applied by the swelled fuel and in response to the dilatation accompanying precipitate growth, is an important parameter for correct simulation and more rigorous models with evolving micromechanics will be developed in the near future.

This model has been extensively verified and validated for simulating microstructural evolution coupled to compositional changes, including grain growth, phase transformation, nucleation and growth of a second phase, and Fickian diffusion. Furthermore, the developments and adaptations made for simulating hydride precipitation have been thoroughly verified to correctly simulate the materials processes claimed in this work. However, validation has been limited to qualitative comparisons to known behavior in claddings. This is primarily a consequence of the limited knowledge in hydride precipitate formation. Formulating a validation strategy and demonstrating the hydride model capability quantitatively are priorities for the work proposed in FY14.

Almost all the simulations presented in this report were carried out using software built on the platform SPPARKS (Plimpton et al., 2009), a Sandia code designed for particle-based kinetic Monte Carlo simulations. This code is written in standard C++ and can run on virtually any UNIX machine with parallel or serial computing capability. The code for the hydride simulations is built within the SPPARKS framework. Most of the simulations reported in this work were performed on a desktop Apple Mac Pro with 12 processors. The simulations shown in this report took typically between 10 and 50 minutes with 6 to 12 processors.

## CONTENTS

SUMMARY .....	v
CONTENTS.....	vii
FIGURES .....	vii
ACRONYMS .....	x
1.0 MODEL DEVELOPMENT .....	1
1.1 Microstructure Generation.....	3
1.2 Thermodynamic Calculations for the Zirconium – Hydrogen Binary System.....	7
1.3 Development and Adaptation of Hybrid Model to Simulate Hydride Formation.....	11
1.4 Zirconium Hydride Precipitation.....	12
2.0 SIMULATION OF HYDRIDE PRECIPITATION .....	16
3.0 SUMMARY AND CONCLUSIONS .....	25
REFERENCES.....	26

## FIGURES

Figure 1. ZrH precipitates in zircaloy cladding have a characteristic morphology. They align themselves to form platelets in the circumferential direction of the cylindrical clad.....	2
Figure 2. The ZrH precipitates have oriented themselves in the radial direction due to the hoop stresses present in the clad.....	2
Figure 3. The relative scale of the hydride model is shown here. The optical image shows the cladding dimensions with a thickness of 6 mm. The SEM image showing grain structure has dimension of 130 x 80 $\mu\text{m}$ and the simulations demonstrated in this work have dimension of 30 x 30 x 30 $\mu\text{m}$ . .....	3
Figure 4. Electron backscatter diffraction (EBSD) image showing a typical grain structure of Zircaloy-4 (Qin et al., 2011). .....	4
Figure 5. Texture of a hot-rolled and annealed Zry-4 plate represented by experimental basal $\{0002\}$ and prism $\{10\bar{1}0\}$ and $\{11\bar{2}0\}$ pole figures, with the rolling direction (RD), transverse direction (TD) and normal direction (ND) indicated (adapted from Wang et al., 2013). .....	5
Figure 6. Synthetically generated microstructure for Zircaloy-4. RD, ND and TD are the rolling direction, normal direction and transverse direction. ....	6
Figure 7. The frequency of basal pole orientation as a function of rotation around the transverse direction, $\theta$ , and the rolling direction, $\phi$ . .....	7

Figure 8. Hexagonal (hcp) Zr structure (different views): (a) in the direction perpendicular to the (0001) axes; (b) in the direction of the (0001) axes. Zr atoms are shown in cyan color; octahedral interstitials are indicated by arrows. ....	8
Figure 9. Positions of single hydrogen in hexagonal (hcp) Zr structure: (b) H in the octahedral interstitial; (c) H in the middle of the Zr-Zr bond. Zr atoms are shown in cyan, and hydrogen in white. ....	8
Figure 10. Relaxed crystalline structures of the three experimentally observed hydrides of zirconium: orthorhombic $\gamma$ -ZrH ( $a=4.592 \text{ \AA}$ ; $c=4.492 \text{ \AA}$ ); cubic $\delta$ -ZrH <sub>1.5</sub> ( $a=4.775 \text{ \AA}$ ) and tetragonal $\epsilon$ -ZrH <sub>2</sub> ( $a=4.999 \text{ \AA}$ ; $c=4.433 \text{ \AA}$ ). ....	9
Figure 11. The Gibbs free energy of the several co-existing phases in the Zr-H system as a function of the hydrogen mole fraction at 800 K. The light blue curve, labeled 3, and the dark blue curve, labeled 4, are the free energies of the phases of interest, namely $\alpha$ -Zr and $\delta$ -ZrH <sub>1.5</sub> . ....	9
Figure 12. Portion of the Zr-H phase diagram showing a detailed view at the Zr-rich region. ....	10
Figure 13. Free-energy curves for the Zr-H system at 300 °C. ....	10
Figure 14. Growth of hydride precipitates in a single crystal of $\alpha$ -Zr. The same precipitates are shown from two different directions. ....	15
Figure 15. Estimated cladding temperature after drying during dry-storage (Hansen, 2012). ....	16
Figure 16. Starting microstructure for the hydride precipitation simulations. ....	17
Figure 17. All in the precipitates in the polycrystalline are imaged and shown from two different angles. ....	18
Figure 18. The same simulation was run with a uni-axial, constant stress applied. ....	18
Figure 19. Precipitation size distribution in a polycrystalline Zr-matrix with randomly oriented grains for the case of no applied stress and application of a constant, uni-axial stress. The same data are shown on a log- and normal-plots. The log plot shows the data more clearly for larger needle sizes and the linear plot shows the data more clearly for the smaller shorter needles. ....	18
Figure 20. Input microstructure with basal orientation stochastically assigned using Eq. 1 for small simulations with seven grains. The grains are elongated in the X-direction, which is also the rolling direction for the purposes of this illustration. ....	19
Figure 21. a, b, and c. Nucleation and growth of $\delta$ -ZrH <sub>1.5</sub> precipitates at time = 3, 27 and 520 Monte Carlo Steps (MCS). Nucleation sites are predominantly at grain boundaries, which is very clearly illustrated in d, e and f, where the same precipitates seen in a, b and c are imaged, but now looking down the rolling direction. The inset between c and f is provided to show the grain boundaries at the surface of the sample and is the same microstructure shown in Figure 20. ....	20
Figure 22. The distribution of hydrogen in the microstructure; hydrogen concentrations are highest in the $\delta$ -ZrH <sub>1.5</sub> precipitates and the matrix is depleted. ....	21
Figure 23. A slice through the microstructure shown in Figures 21 & 22. In a, the grain structure shown in blue with red precipitates and, in b, the composition corresponding to this slice. The red in b are regions of high hydrogen content, which is where the precipitates are located. ....	22

Figure 24. Nucleation of precipitation in this simulation occurs with equal probability in any location. Precipitates at time = 5 and 330 MCS are shown here. The subsequent growth is controlled by diffusion ..... 23

Figure 25. The distribution of hydrogen in the microstructure for the simulation results shown in Figure 24..... 23

Figure 26. A comparison of total precipitate formation for the two cases where nucleation occurs randomly with uniform probability anywhere in the grains and nucleation occurs preferentially at the grain boundaries. .... 24

## ACRONYMS

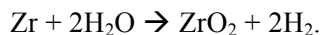
3D	three-dimensional
CALPHAD	CALculation of PHAse Diagrams
DFT	density functional theory
EBSD	electron backscatter diffraction
GGA	generalized gradient approximation
HAZ	heat-affected zone
MCS	Monte Carlo Steps
ND	normal direction
ODF	orientation distribution function
RD	rolling direction
TD	transverse direction
UFD	used fuel disposition
Zry-4	Zircaloy-4

# **MODEL FOR SIMULATION OF HYDRIDE PRECIPITATION IN ZR-BASED USED FUEL CLADDINGS: A STATUS REPORT ON CURRENT MODEL CAPABILITIES**

## **1.0 MODEL DEVELOPMENT**

The US's current used fuel management policy may require ensuring the containment of radioactive materials during storage and subsequent transport for an indeterminately long period. One of the barriers available for fuel confinement is the Zr-based cladding. Ensuring the structural integrity of the cladding is a key component in developing the technical basis for long-term dry-storage. The precipitation and growth of zirconium hydrides during dry-storage is one of the potential fuel rod integrity failure mechanisms by either embrittlement or delayed hydride cracking of the cladding (Hanson et al, 2011). While the phenomenon is well documented and identified as a potential failure mechanism during long-term dry-storage (Birk et al., 2012; NUREG CR-7116; 2011), the ability to actually predict the formation of hydrides is poor. The model described and demonstrated in this document is being developed as a tool to predict hydride formation during long-term dry storage.

The formation of hydride precipitates in clad is a well-known and well-documented phenomenon. The zircaloy cladding oxidizes while in the reactor as



This reaction produces a surface oxide layer and H<sub>2</sub> gas. Some portion, estimated to be 5 to 20%, of the hydrogen gas released by this reaction is absorbed by the clad and diffuses into the clad. The absorption process is typically called hydrogen uptake. Depending on the alloy composition, temperature and amount of H absorbed, the H can stay dissolved in the cladding or it can precipitate forming zirconium hydride precipitates when the solubility limit is exceeded.

The morphology of the ZrH<sub>x</sub> precipitates that form during service in reactor is characterized by needles aligned as shown in Figure 1 (Hanson et al., 2011; Birk et al., 2012). The hydride is thought to precipitate at defects and grain boundaries that are preferentially aligned along the circumferential direction of the clad as shown in Figure 1. The circumferentially oriented hydrides form in reactor when the internal stress applied by the swelling fuel is countered by the coolant pressure. When the used fuel rods have completed their service life, they are stored in cooling pools for some years. When the storage pool approaches capacity, the assemblies are transferred to dry storage casks where they go through a drying operation either through vacuum drying or forced helium backfill. During the drying stage, due to the temperature increase, some of the hydride precipitates, shown in Figure 1, redissolve into the zircaloy clad. Upon cooling and subsequent dry-storage, the hydrides reprecipitate but are reoriented along the radial direction as shown in Figure 2. The alignment is due to the stress state of the clad. With the coolant no longer applying a compressive stress, the swelled fuel pellets cause a tensile hoop stress in the clad. The hydride precipitates form perpendicular to this hoop stress. This orientation is undesirable as the oriented precipitates act as stress concentrators and may lead to fracture of the clad during long-term storage.

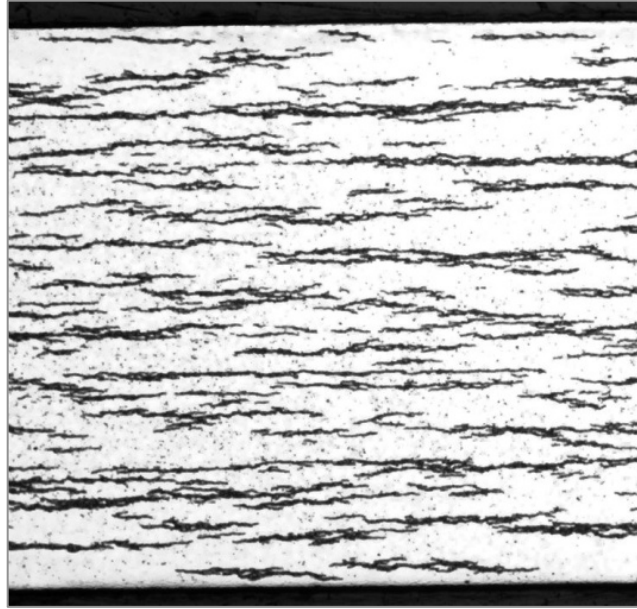


Figure 1. ZrH precipitates in zircaloy cladding have a characteristic morphology. They align themselves to form platelets in the circumferential direction of the cylindrical clad.

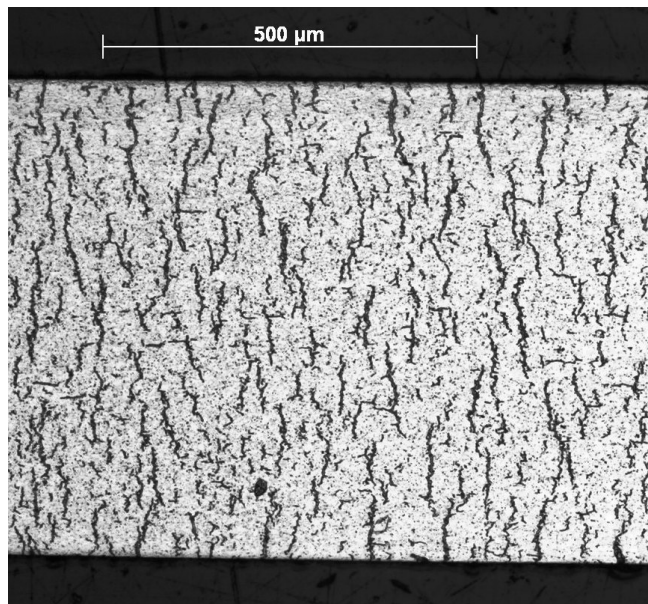


Figure 2. The ZrH precipitates have oriented themselves in the radial direction due to the hoop stresses present in the clad.

The objective of this computational tool is to develop capabilities for predicting hydride precipitation in the claddings of used fuel rods after removal from cooling pools during an indeterminately long period of dry-storage. The heat treatment to dry the fuel, which is just below 400 °C for 24 hours (Hansen et al., 2011), dissolves some or all of the hydrides that may have formed during reactor service and storage in cooling pools. The extent of dissolution depends on the claddings composition, amount of hydrogen pick-up, and the time and temperature of drying (Kearns, 1967; Colas et al, 2010). For our demonstration, we assume that the starting condition of the cladding is that all the hydrogen present is dissolved in the

zirconium matrix. As the temperature of the cladding gradually cools, the hydrogen content in the cladding exceeds its solubility limits. At this point, the zirconium hydride precipitates. This phase transformation is thought to be a nucleation and growth transformation, with the diffusion of hydrogen to the precipitates controlling the growth of the precipitates. The underlying microstructure with nucleation sites and growth characteristic of the cladding is necessary to simulate hydride formation.

A key feature of these meso-scale microstructural simulations is the length scale of the simulations. Figure 3 puts the model scale capabilities in perspective. The scale of the model is shown with respect to the cladding dimensions. The cladding thickness is 600 mm, the grain size of Zry-4 grains is 10  $\mu\text{m}$  and the simulation scale is 30  $\mu\text{m}$  on one edge. The model is demonstrated on a small polycrystalline portion of the clad using a desktop Apple Mac Pro with 12 processors. The production run used to obtain engineering scale behavior will be performed on large parallel cluster machines using claddings of 100 to 200  $\mu\text{m}$  on an edge, which are approximately the size of the SEM photo showing grains in Figure 3.

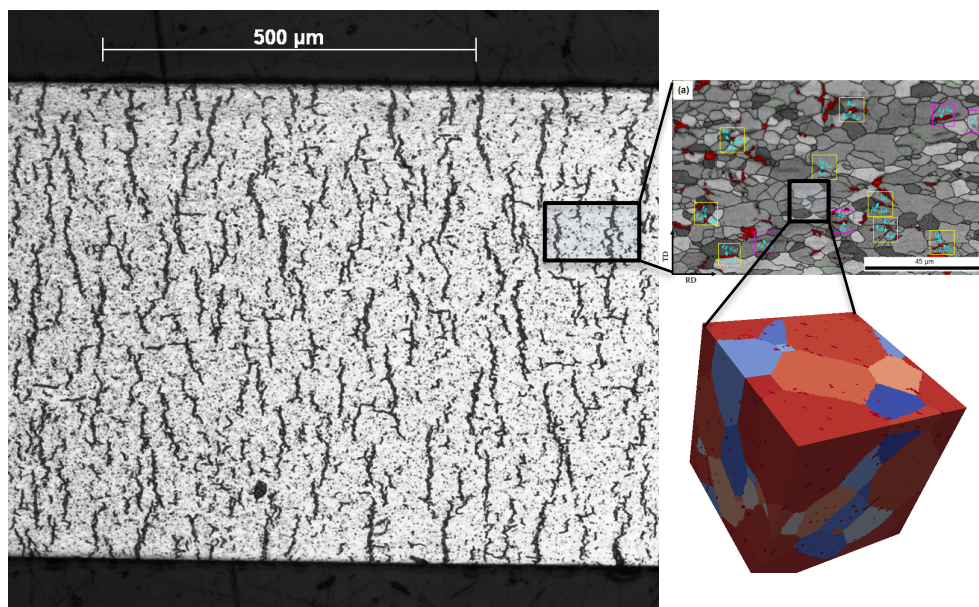


Figure 3. The relative scale of the hydride model is shown here. The optical image shows the cladding dimensions with a thickness of 6 mm. The SEM image showing grain structure has dimension of 130 x 80  $\mu\text{m}$  and the simulations demonstrated in this work have dimension of 30 x 30 x 30  $\mu\text{m}$ .

## 1.1 Microstructure Generation

The microstructure chosen for this demonstration is a Zircaloy-4 microstructure. A three-dimensional (3D) grain structure with crystallographic texture and grain elongation was generated using the information obtained from the published literature. Limited information on the grain size and shape of Zircaloy-4 is available due to the difficulty of etching and imaging zirconium (Danielson and Sutherlin, 2004). However, some data is available (Qin et al., 2011; Kumar et al., 2010; Santisteban et al., 2010; Abe, 2010). These show a slightly elongated grain structure in the rolling direction, with a nominal grain size of approximately 10  $\mu\text{m}$ . One of the best examples found in the literature is shown below in Figure 4. Characterization of this image and other examples found showed an average elongation of approximately 2x in the rolling direction.

**4**

The pilgering process used to form Zr-based claddings imparts not only grain shape texture, but also crystallographic texture as the rolling processes compress the sheet in the normal direction and constrain it in the transverse direction, so that the basal poles tend to be parallel to the normal direction. Surprisingly, significantly more data exist on the crystallographic texture of Zircaloy-4 and it is sufficiently quantified to implement into synthetically generated microstructures. The crystallographic texture is described by Kearns numbers for the three principal directions in the Zircaloy samples, i.e.  $f_N$  (normal),  $f_T$  (transverse) and  $f_R$  (rolling), defined as a weighted average of the intensity of the basal plane normals oriented with respect to the sample's principal direction; the sum of the Kearns number is  $f_N + f_T + f_R = 1$ . Kearns numbers calculated from orientation distribution function (ODF) texture data obtained at 100 °C by neutron diffraction for as-manufactured Zircaloy-4 are:  $f_N = 0.54$ ,  $f_T = 0.28$  and  $f_R = 0.18$  (Fong, 2013). These values are in close agreement with the Kearns numbers for as-received Zircaloy-4 determined earlier by Coleman and coworkers using X-ray diffraction methods, i.e.  $f_N = 0.56$ ,  $f_T = 0.29$  and  $f_R = 0.15$  for Atucha claddings and  $f_N = 0.65$ ,  $f_T = 0.30$  and  $f_R = 0.05$  for Ziratec claddings (Coleman, 2010).

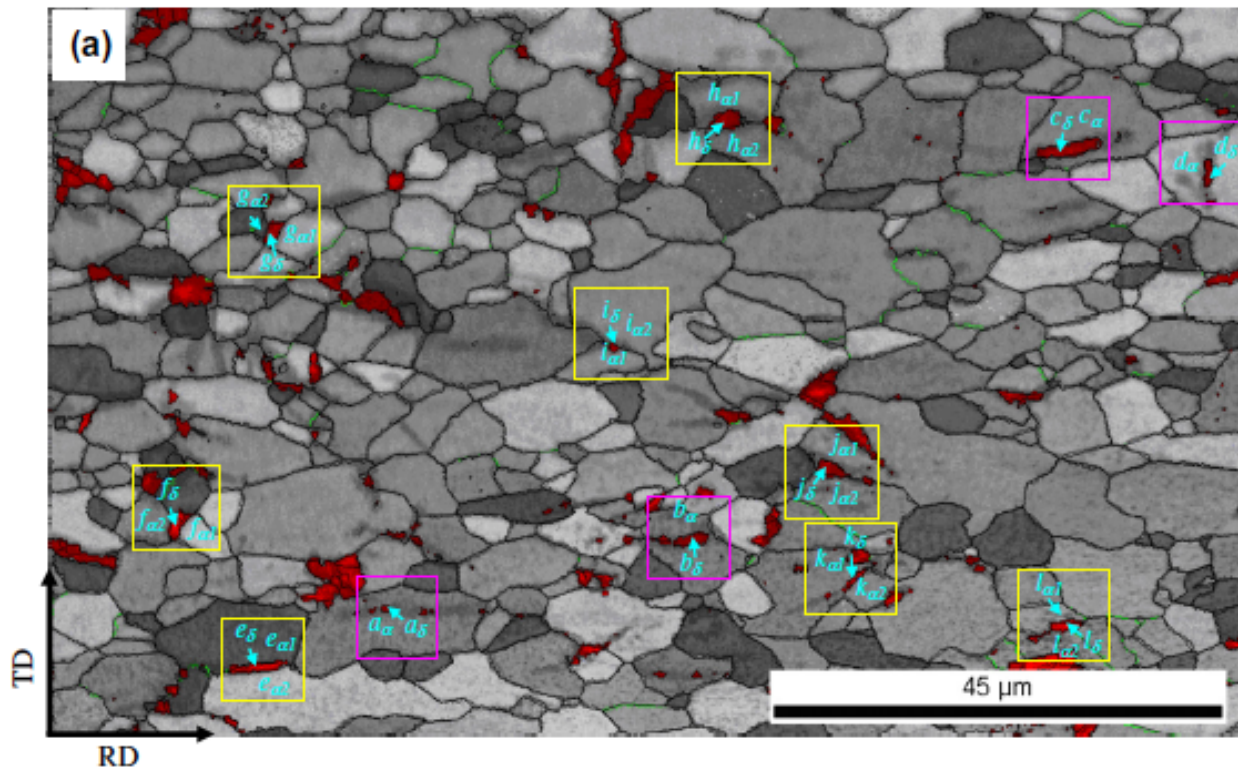


Figure 4. Electron backscatter diffraction (EBSD) image showing a typical grain structure of Zircaloy-4 (Qin et al., 2011).

Although the three-dimensional strain history of fabrication will ultimately play a role in their texture and properties and the subsequent formation of oriented hydrides within the Zr matrix (Louthan & Marshall, 1963; Kearns & Woods, 1966; Marshall, 1967), the similarity between Kearns numbers strongly suggests that all these Zircaloy-4 claddings have the same type of texture. X-ray and electron back-scattering diffraction studies (Kiran Kumar et al., 2010), as well as neutron scattering investigations (Wang et al., 2013; Fong, 2013), have shown that typical cold-worked and stress-relieved or hot-rolled and annealed Zircaloy-4 claddings are characterized by a strong (0002) basal plane texture, with double pole maxima inclined typically by ca.  $\pm 30^\circ$  from the normal direction (ND) and extended along the transverse direction (TD), while a preferential  $\{10\bar{1}0\}$  prismatic orientation is seen along the rolling direction (RD) as shown in Figure 5. The basal pole orientation of Zircaloy-4 appears to differ only slightly with manufacturing process variables, such as the number of cold reductions and intermediate anneals (Fong, 2013).

Other evidence to show that texture in the different Zircaloy-4 claddings is similar is the Hill numbers. From the ODF texture data, the three mechanical tensile anisotropic factors proposed by Hill and designated as  $F$ ,  $G$ , and  $H$  can be derived (Hill, 1948). For isotropic materials,  $F = G = H = \frac{1}{2}$ . Fong (Fong, 2013) determined Hill's anisotropy factors from the neutron-diffraction ODF of as-manufactured Zircaloy-4:  $F = 0.76$ ,  $G = 0.54$  and  $H = 0.20$ . Hunt and Newell (Hunt, 1975; Hunt & Newell, 1979), reported very similar Hill's numbers for the Zircaloy-4 that they examined:  $F = 0.76$ ,  $G = 0.56$  and  $H = 0.18$ .

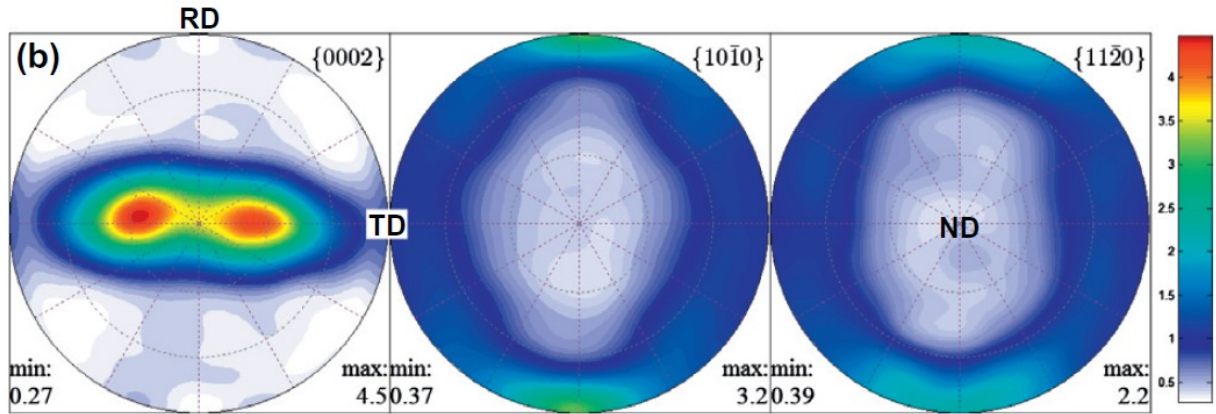


Figure 5. Texture of a hot-rolled and annealed Zry-4 plate represented by experimental basal  $\{0002\}$  and prism  $\{10\bar{1}0\}$  and  $\{11\bar{2}0\}$  pole figures, with the rolling direction (RD), transverse direction (TD) and normal direction (ND) indicated (adapted from Wang et al., 2013).

While not directly relevant for the current model, this discussion on welded regions of the cladding is included. Several recent neutron radiography experiments showed that the texture and microstructures of Zircaloy-4 matrix can be modified locally by the welding and brazing processes used to assemble the fuel bundle (Santisteban et al., 2012; Fong, 2013). The “heat-affected-zone” (HAZ) of Zircaloy-4 heated to 850 °C for typically less than a minute usually features  $\alpha$ -annealed equiaxed microstructures, while in the areas where brazing of appendages involves heating up to about 1050 °C,  $\beta$ -transformed Zr microstructures are observed (Fong, 2013). Apart from producing an equiaxed grain structure, little to no change to the grain structure is observed in the  $\alpha$ -annealed HAZ material, as shown by its estimated Kearns numbers  $f_R = 0.53$ ,  $f_T = 0.28$  and  $f_L = 0.19$  and Hill's anisotropy factors  $F = 0.73$ ,  $G = 0.56$  and  $H = 0.21$  for the resulting texture. However, high-temperature brazing cycles leading to  $\beta$ -transformed microstructures induce a change in texture from a predominant radial character to a mix of radial and non-radial characteristics (Fong, 2013). This can be seen in the noticeable departure of the Kearns numbers for the  $\beta$ -transformed texture, i.e.,  $f_R = 0.51$ ,  $f_T = 0.26$  and  $f_L = 0.24$ , and the Hill's anisotropy factors  $F = 0.58$ ,  $G = 0.54$  and  $H = 0.38$ , compared to the as-manufactured Zry-4 texture and properties.

Based on these data, a synthetic microstructure, shown in Figure 6, was generated using Dream3D (Jackson, 2013). The rolled synthetic microstructure had an average grain size of 10  $\mu\text{m}$  with a standard deviation of 1  $\mu\text{m}$ . While there is very little data on grain size, there is even less on grain size distributions and their standard deviations. Thus, the choice of standard deviation is estimated from existing knowledge of rolled metals. The average elongation in the rolled direction of the synthetic microstructure is also 2x as compared to the transverse and normal directions; this is based on simple measurements of the microstructures from the published literature.

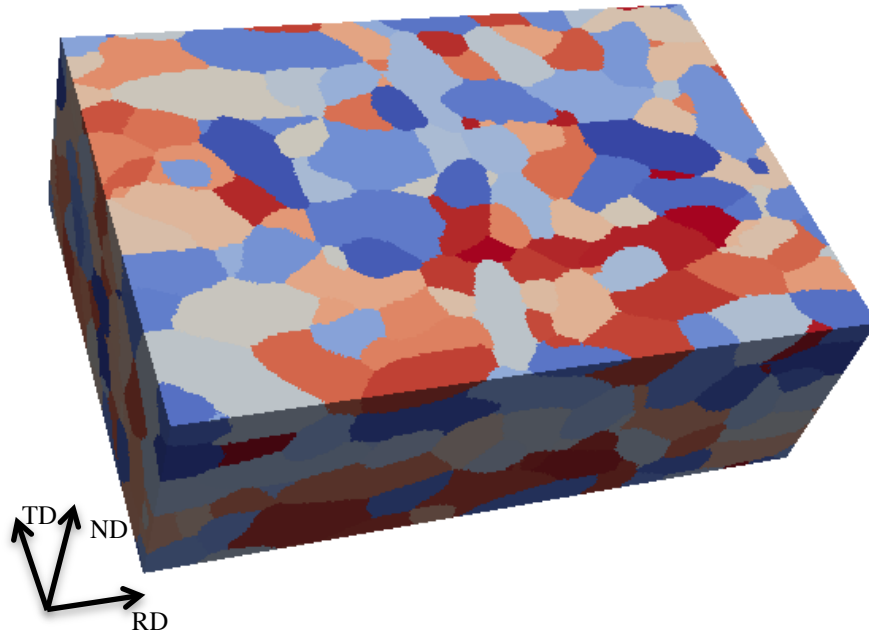


Figure 6. Synthetically generated microstructure for Zircaloy-4. RD, ND and TD are the rolling direction, normal direction and transverse direction.

The orientations of the grains were assigned stochastically using the information from the Kearns numbers. As noted earlier, the three Kearns numbers give the weighted average of the intensity of the basal plane normals oriented in the three principal directions. Based on the data presented above, we estimate the frequency ratio of grain basal poles pointing in the normal to transverse to rolling directions to be 3 : 1.5 : 1. A function to approximate these frequency ratios with the overall characteristics shown in Figure 5 was constructed as

$$F = 0.9 + \frac{(.00515(\phi - 5)^3 - (\phi - 19)^2)\cos(0.78\theta)}{1169} \quad \text{Eq. 1}$$

where  $\theta$  is the rotation around the transverse direction axis and  $\phi$  is the rotation around the rolling direction axis. This function is plotted in Figure 7. This distribution is similar to the characteristics given in Figure 5, but the plotting coordinates are different; Figure 5 shows pole projections, while Figure 7 is plotted on orthogonal axes. The basal plane orientation with the highest frequency of occurrence is at  $\theta = 30^\circ$  and  $\phi = 0^\circ$ . This estimate is for model demonstration purpose and will be refined and adjusted for the various Zircaloy-4 as more specific information becomes available.

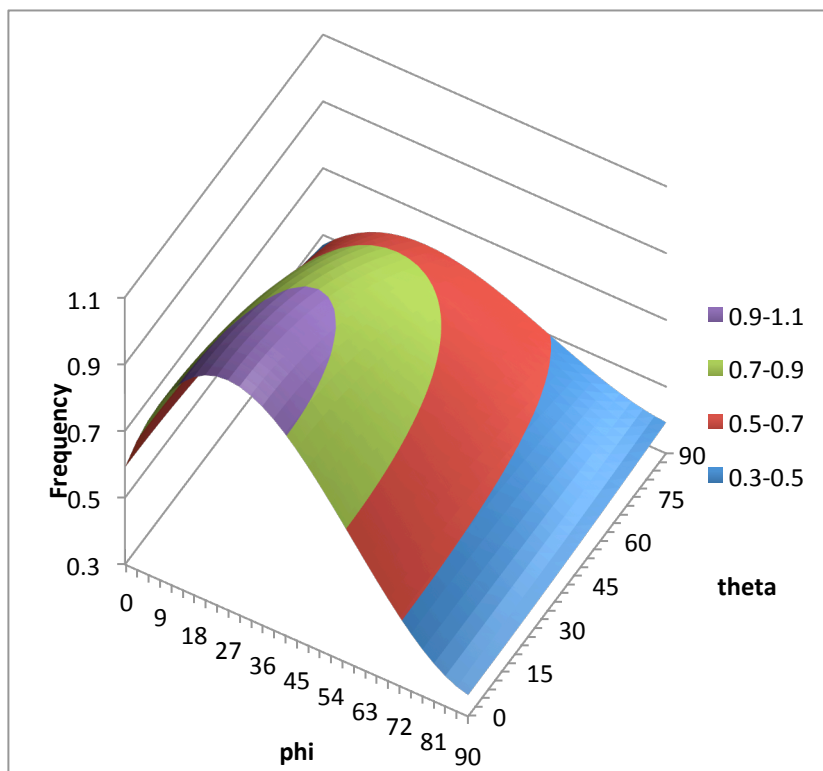


Figure 7. The frequency of basal pole orientation as a function of rotation around the transverse direction,  $\theta$ , and the rolling direction,  $\phi$ .

## 1.2 Thermodynamic Calculations for the Zirconium – Hydrogen Binary System

The model requires free energies for each phase as functions of its components. Since, we are only considering the two components, Zr-H, in the composition and temperature ranges of interest for nuclear fuel applications, the crystal structure and free energies were calculated using *ab initio* calculations using density functional theory (DFT) and computational thermodynamics using CALPHAD-type (CALculation of PHase Diagrams) calculations. The supercell total-energy calculations with DFT were used to determine the crystalline structure of the various Zr-H phases. The DFT calculations were based on the generalized gradient approximation (GGA) for exchange and correlation, and plane waves (Payne et al, 1992). A more detailed description of the computational DFT work is provided in a separate report (Glazoff, 2013).

A self-consistent description of phase equilibria in multi-component systems and thermodynamic properties of materials was used to bridge between phase equilibria and thermodynamic properties of Zr-H. In this work, commercial databases for zirconium alloys TTZR1 (ThermoTech Ltd.) and binary alloys TCBIN (ThermoCalc AB) were used. These databases and the ThermoCalc version S software were used to generate data on the thermodynamic properties of hydrides, in particular, partial molar enthalpy and entropy of hydrogen. The obtained results were consistent with the constructed phase diagrams and property diagrams. All results were critically evaluated in light of the existing experimental data.

The equilibrium crystalline structures of hcp-Zr and its three hydrides are depicted in Figures 8 and 9, respectively. In all cases, the equilibrium lattice parameters were determined by total-energy relaxation technique of the lattice parameters and corresponding atomic positions.

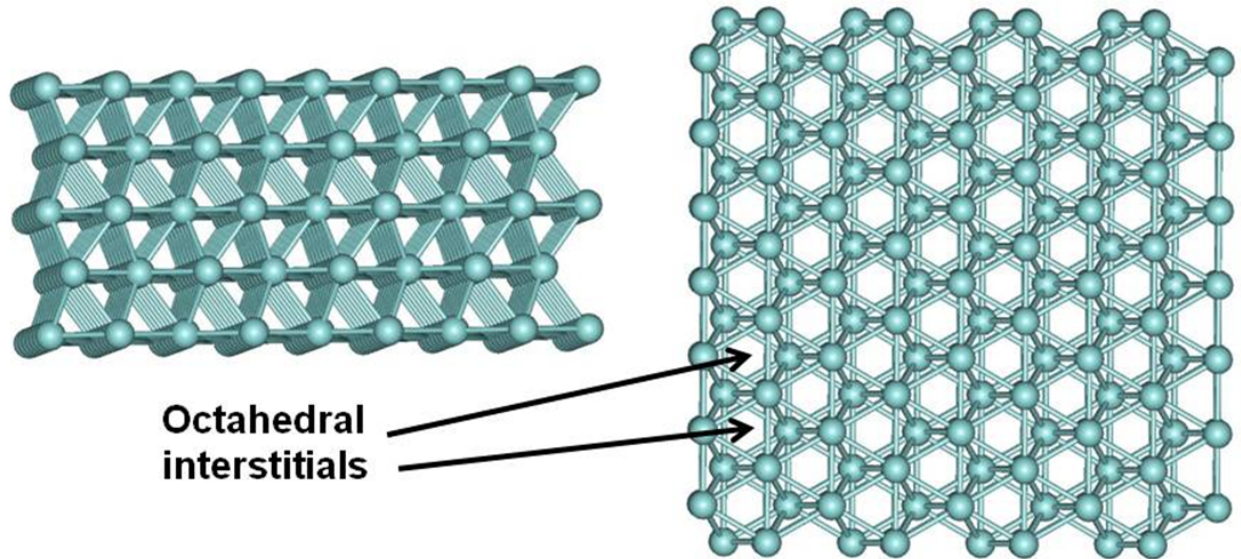


Figure 8. Hexagonal (hcp) Zr structure (different views): (a) in the direction perpendicular to the (0001) axes; (b) in the direction of the (0001) axes. Zr atoms are shown in cyan color; octahedral interstitials are indicated by arrows.

The low-temperature  $\alpha$ -phase of Zr has hcp structure characterized by the 2/1 ratio of tetrahedral and octahedral interstitial positions per unit cell. The lattice parameters were determined in this work as  $a = 3.2276 \text{ \AA}$  and  $c = 5.1516 \text{ \AA}$ , space group  $P63/mmc$  (see Figure 8). These results are in excellent agreement with the experimental data reported in the previous section.

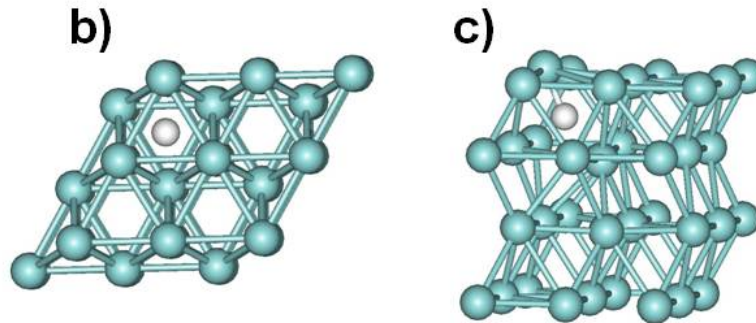


Figure 9. Positions of single hydrogen in hexagonal (hcp) Zr structure: (b) H in the octahedral interstitial site; (c) H in the middle of the Zr-Zr bond. Zr atoms are shown in cyan, and hydrogen in white.

There are three distinctly different types of zirconium hydride structures described in the literature:  $\gamma$ -ZrH,  $\delta$ -ZrH<sub>1.6-1.7</sub> (which was modeled in this work as ZrH<sub>1.5</sub>) and  $\epsilon$ -ZrH<sub>2</sub> (Blomquist et al., 2010). In Figure 10, the results of first-principles calculations yielding the three relaxed crystal lattice structures are presented. Again these results are in excellent agreement with those reported in the literature.

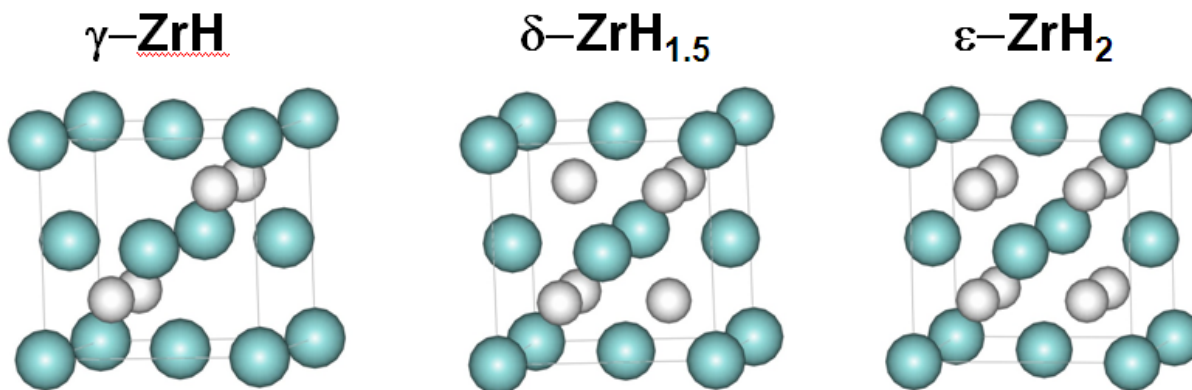


Figure 10. Relaxed crystalline structures of the three experimentally observed hydrides of zirconium: orthorhombic  $\gamma$ -ZrH ( $a=4.592$  Å;  $c=4.492$  Å); cubic  $\delta$ -ZrH<sub>1.5</sub> ( $a=4.775$  Å) and tetragonal  $\epsilon$ -ZrH<sub>2</sub> ( $a=4.999$  Å;  $c=4.433$  Å).

The values of the Gibbs free energy computed at  $T=800$  K are illustrated in Figure 11; these values lie in the range from  $-20,000$  J/mol to  $\sim 8,000$  J/mol. This reference range will be useful when we discuss existing data on partial molar enthalpy of hydrogen in different zirconium alloys, as well as for determining the driving forces of hydride formation. The corresponding look-up tables were used for phase-field calculations of zirconium hydride microstructure evolution by fitting these tabulated data.

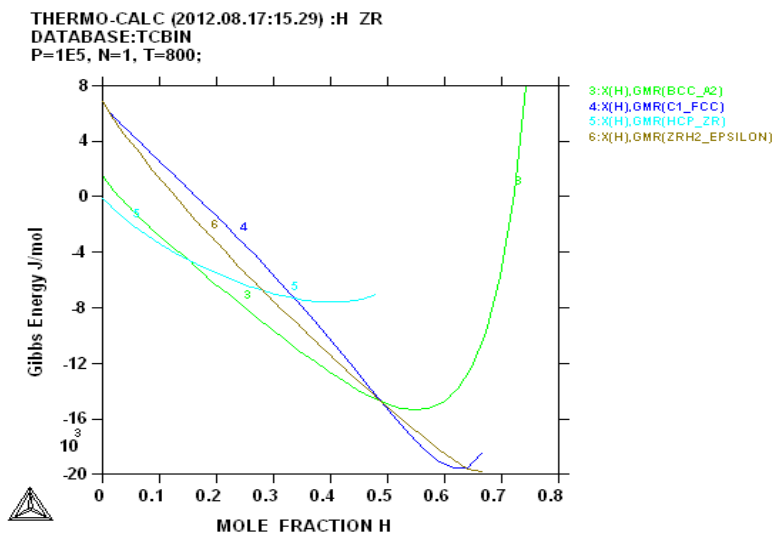


Figure 11. The Gibbs free energy of the several co-existing phases in the Zr-H system as a function of the hydrogen mole fraction at 800 K. The light blue curve, labeled 5, and the dark blue curve, labeled 4, are the free energies of the phases of interest, namely  $\alpha$ -Zr and  $\delta$ -ZrH<sub>1.5</sub>.

The magnified diagram for the hydrogen mole fraction varying from 0 to 0.1 is given in Figure 12. It provides an estimate of the hydride dissolution temperature as  $550^\circ\text{C}$  corresponding to  $\sim 0.054$  mole fraction of hydrogen. Also, a distinctive feature of this diagram is the retrograde solubility above  $550^\circ\text{C}$ , with a minimum corresponding to  $\sim 600^\circ\text{C}$ . Again, these results correspond well to the existing experimental data (Ostberg, 1962; Yamanaka et al., 1997; Zuzek et al., 1990) giving confidence in the thermodynamic calculations.

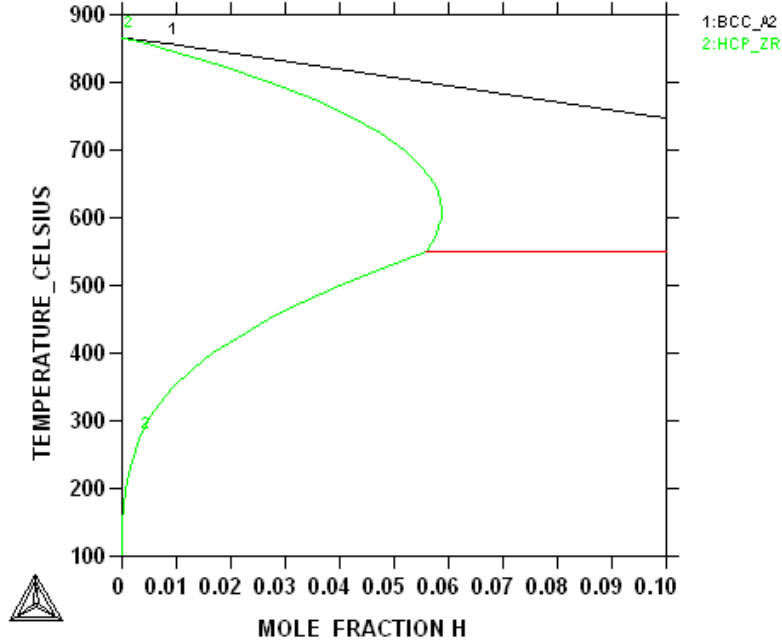


Figure 12. Portion of the Zr-H phase diagram showing a detailed view at the Zr-rich region.

The free energy data for the  $\alpha$ -Zr and  $\delta$ -ZrH<sub>1.5</sub> phases at 300 °C were fitted using polynomials of the fifth order as shown in Figure 13.

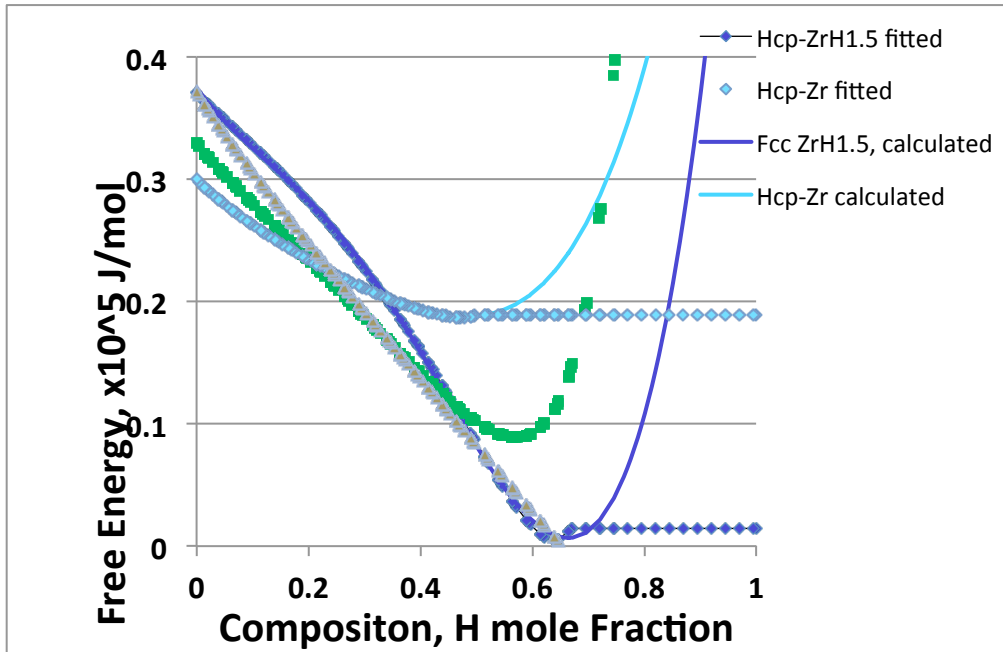


Figure 13. Free-energy curves for the Zr-H system at 300 °C.

The fitted free energy functions at 300 °C are:

$$E_{\alpha-Zr} = 2.135026x^5 - 16.96998x^4 + 7.119466x^3 - 1.541714x^2 - 0.297439x + 0.3679003$$

Eq. 2

for the  $\alpha$ -Zr phase, and

$$E_{\delta\text{-ZrH}_{1.5}} = 2.135026x^5 - 0.6183701x^4 - 0.6586253x^3 + 0.6083004x^2 - 0.4182968x + 0.2992497 \quad \text{Eq. 3}$$

for the  $\delta\text{-ZrH}_{1.5}$  phase. The free energies for  $\gamma\text{-ZrH}$  and  $\epsilon\text{-ZrH}$  are included for completeness, but not used for the demonstration purposes of this report.

### 1.3 Development and Adaptation of Hybrid Model to Simulate Hydride Formation

The hybrid Potts-phase field model was applied to simulate the nucleation and growth of  $\delta\text{-ZrH}_{1.5}$  precipitates. The model will not be described in this report as a detailed description can be found readily (Homer et al., 2013; Tikare and Homer, 2012; Tikare and Schultz, 2012). However, the model was further developed and adapted to treat this application extensively. These developments will be described in this section. The equation of state used by the hybrid is

$$E_{hyb} = \sum_{i=1}^N \left( E_v(q_i, C) + \frac{1}{2} \sum_{j=1}^n J(q_i, q_j) \right) + E_i \quad \text{Eq. 4}$$

where the volumetric free energy is given by Eqs. 2 & 3 for the  $\alpha\text{-Zr}$  and  $\delta\text{-ZrH}_{1.5}$  phases  $q$ , respectively. The interfacial energy is given by unlike neighbors in the Potts formulation and, as described later, compositional gradients in the phase field formulation  $E_i$ . The kinetic equation governing evolution in the phase field is explained further here as it differs from those used in the past applications of the phase field or hybrid models. This change was motivated to ensure that the model can be developed to incorporate more complex chemistry and phases of Zircalloys, as this information is generated. The evolution of composition is given by

$$\frac{\partial C}{\partial t} = \nabla \cdot M \nabla \frac{\delta E}{\delta C} \quad \text{Eq. 5}$$

where  $C$  is the phase-field representing the composition,  $M$  is the mobility and  $E$  is the free energy defined in Eq. 4 and  $t$  is time. For a binary system with two components and two phases, the volumetric free energy of the system may also be defined as

$$E_v = \mu_1 C_1 + \mu_2 C_2 \quad \text{Eq. 6}$$

Using mass conservation  $C_1 + C_2 = 1$  and substituting for in Eq. 6, one gets

$$\frac{\partial E_v}{\partial C_2} = (\mu_2 - \mu_1) \quad \text{Eq. 7}$$

When the free energy is known, the chemical potentials of the component 1 and 2 in a given phase can be shown to be

$$\mu_1 = E - \frac{\partial E}{\partial C_2} C_2$$

$$\mu_2 = E + (1 - C_2) \frac{\partial E}{\partial C_2} \quad \text{Eq. 8}$$

In addition to the volumetric free energy, an interfacial free energy  $E_i$  term exists in the traditional phase field model

$$E_i = \kappa (\nabla C)^2 \quad \text{Eq. 10}$$

The variational derivative of the total free energy with respect to composition is

$$\frac{\delta E}{\delta C} = \mu + \kappa \nabla^2 C \quad \text{Eq. 11}$$

To reiterate, the complete definition of the chemical potential is used in Eq. 8 in anticipation of additional components and phases to be treated in the future. Thus, evolution of the composition is treated by Eq. 5 using the variational derivative in Eq. 11 with the free energies of the two phases given by Eqs. 2 & 3.

The microstructures of the zircaloy matrix and hydride precipitates are evolved using Monte Carlo Potts techniques. The microstructural feature or state is identified by a unique integer identifier  $q$  that designates a discrete quantum of material of a particular orientation and phase occupying that site. This set of states  $q$ 's evolves to simulate microstructural evolution to minimize the overall free energy of the system along particular microstructural paths. Individual changes to the state  $q$  at all the sites are attempted. The change is carried out using the Metropolis algorithm. The probability of the change  $P$  is calculated using Boltzmann statistics, where the probability of change is a function of the change in energy  $\Delta E$ , i.e.,

$$P = \exp\left(-\frac{\Delta E}{k_B T}\right) \quad \text{for } \Delta E > 0$$

$$P = 1 \quad \text{for } \Delta E \leq 0 \quad \text{Eq. 12}$$

The change in energy,  $\Delta E = E_{final} - E_{initial}$ , is calculated using Eq 4. If the probability  $P = 1$ , the change is carried out. If  $P < 1$ , then a random number  $R$  that is evenly distributed from 0 to 1 is chosen. If  $R \leq P$ , then the site is changed to its new state. In this way, the microstructure is evolved, while it is directly coupled to the compositional evolution through the equation of state given by Eq. 4. The units of time in the simulations are Monte Carlo steps, MCS; 1 MCS is when each site in the simulation has attempted a change.

The hydride growth and reorientation model is built as an extension module for SPPARKS. SPPARKS is an acronym for stochastic parallel particle kinetic simulator. SPPARKS is a KMC code that has algorithms for both rejection-free KMC and rejection KMC also called Metropolis Monte Carlo (Plimpton et al., 2009). SPPARKS is distributed as an open source code. It is highly versatile, supports a number of different applications, can be extended to add new functionalities and is able to run in serial or in parallel. The parallel version uses the message-passing interface (MPI) to perform concurrent computations over all processors, while minimizing communication overhead between processors. The necessary solvers for treating the partial differential equation Eq. 5 are incorporated into the hydride extension module within SPPARKS.

## 1.4 Zirconium Hydride Precipitation

In Section 1.2, the first-principles and thermodynamic calculations show three phases of zirconium hydride with free energies that are close together, as seen in Figure 11. Their minima occur at similar compositions and the free energy curves intersect with no hydride phase having a dominant energy advantage over the others. The free energies for  $T = 300, 350$  and  $400$  °C are very similar. Furthermore, all three phases have been observed under different conditions and there are some contradictory data suggesting that  $\delta\text{-ZrH}_{1.5}$  may not be the hydride phase that is precipitating as described later in this section. After careful review of the published data, for this demonstration, we have chosen to not simulate the  $\gamma\text{-ZrH}$  and  $\varepsilon\text{-ZrH}_2$  phases and thus their free energies and phase structures are not included in the model. However, the thermodynamic data and model capability is being developed, so they can be

included, should the presence and behavior of the  $\gamma$ -ZrH and  $\epsilon$ -ZrH<sub>2</sub> phases become significant to hydriding of Zr-based claddings. This choice to discard  $\gamma$ -ZrH and  $\epsilon$ -ZrH<sub>2</sub> phases is justified in the following.

As already described, at reactor-operating temperature, the zirconium cladding absorbs hydrogen and forms hydride precipitates when the hydrogen solubility limit is exceeded. The zirconium matrix is the hexagonal (hcp)  $\alpha$  phase ( $P63/mmc$ ,  $a = 3.2276 \text{ \AA}$  and  $c = 5.1516 \text{ \AA}$ ) with one Zr atom at (0.333, 0.666, 0.25). For the sake of simplicity, the other alloying elements are ignored. At reactor fuel cladding temperature, which are typically 340 °C at the outer tube diameter and ~370-380 °C at the inner tube diameter, the hydrogen solubility ranges between 100-150 wt. ppm (Motta and Chen, 2012).

Below 550 °C, three hydride phases have been experimentally observed in the phase diagram of the zirconium-hydrogen system over the composition range 0-60 at.% of hydrogen: the stable face-centered cubic (fcc)  $\delta$ -ZrH<sub>1.6-1.7</sub> typical has Zr/H ratio of ~1.66 (CaF<sub>2</sub> prototype structure with space group  $Fm\bar{3}m$ ;  $a = 4.778 \text{ \AA}$ ;  $V = 109.07 \text{ \AA}^3$ ) (Beck, 1962), the stable face-centered tetragonal (fct)  $\epsilon$ -ZrH<sub>1.74-2</sub> (ThH<sub>2</sub> prototype structure with space group  $I4/m\ mm$ ;  $a = 4.9689 \text{ \AA}$ ,  $c = 4.4497 \text{ \AA}$ ) (Zuzek et al., 2000), and the metastable ordered fct  $\gamma$ -ZrH<sub>1.0</sub> (space group  $P4_2/n$ ;  $a = 4.596 \text{ \AA}$ ,  $c = 4.969 \text{ \AA}$ ;  $V = 103.72 \text{ \AA}^3$ ) (Sidhu et al., 1963). More careful characterization by inelastic neutron scattering of ZrD showed that the  $\gamma$ -phase possesses a small orthorhombic distortion (space group  $Cccm$ ;  $a = 4.549 \text{ \AA}$ ,  $b = 4.618 \text{ \AA}$ ,  $c = 4.965 \text{ \AA}$ ) (Kolesnikov et al., 1994). Despite multiple recent attempts to synthesize the pure phase  $\gamma$  (Bashkin et al., 1992; Kolesnikov et al., 1994), no one has successfully produced a bulk specimen consisting entirely of the  $\gamma$ -hydride phase, even when hydrogenating specimens to 1:1 stoichiometric composition of this phase. This observation seems to confirm the metastable character of the  $\gamma$ -hydride phase at temperature below the eutectoid temperature. The fct  $\epsilon$ -hydride phase is usually not formed for hydrogen compositions in zirconium alloys of practical interest in nuclear applications (Puls, 2012), and is therefore not of direct interest for the topic of this report. Recently, it was also suggested by Zhao and coworkers (Zhao et al., 2008) that another metastable coherent trigonal phase dubbed  $\zeta$ , with probable stoichiometry ZrH<sub>0.25-0.5</sub> and ZrH<sub>0.5</sub> being the most frequent composition (space group  $P3m1$ ;  $a = 3.3 \text{ \AA}$ ,  $c = 10.29 \text{ \AA}$ ), could exist based on results from electron precession microdiffraction and electron energy loss spectroscopy, however this phase has not yet been confirmed by other research groups.

The exact nature, role and occurrence of the  $\gamma$  phase within the  $\alpha$ -Zr matrix remains controversial (Lanzani and Ruch, 2004). They reported stable  $\delta$  phase and metastable  $\gamma$  phase differ only in the degree of ordering of the hydrogen atoms on tetrahedral sites, which in turn affects the hydride composition. In the  $\delta$  phase, four H atoms randomly occupy the eight available tetragonal (0.25, 0.25, 0.25) sites, while in the  $\gamma$  phase hydrogen atoms occupy the tetrahedral sites on alternating (110) planes (Zr atoms are at the (0.25, 0.25, 0.25) sites and H atoms at (0, 0, 0) and (0, 0, 0.5)). Metallographic studies of specimens in the composition range ZrH<sub>1.47-1.57</sub> showed that the  $\gamma$ -hydride phase appeared as banded precipitates of lenticular shape embedded in the majority  $\delta$ -hydride phase (Barracough and Beevers, 1970). These specimens showed some structural instability since re-examination of these specimens after 6 months revealed additional  $\gamma$ -hydride precipitates formed at the  $\alpha/\delta$  boundaries while small, globular precipitates of  $\alpha$ -Zr were found at the  $\delta$  grain boundaries (Puls, 2012). The metallographic evidence obtained by Barracough and Beevers indicates that the  $\gamma$ -hydride phase forms in  $\delta$ -hydride by a shear mechanism, with the banded structure indicating that this shear is relieved by alternate twinning of the lattice in opposite directions. The suggestions by both Beck (Beck, 1962), and Barracough and Beevers (Barracough and Beevers, 1970) that the formation of the  $\gamma$ -hydride phase (and the  $\epsilon$ -hydride phase) in  $\delta$ -hydride occurs essentially by a martensitic type transformation are supported by the analyses and experimental results of Cassidy and Wayman (Cassidy and Wayman, 1980a, 1980b). However, in contrast to a strictly diffusionless martensitic transformation, these invariant plane strain transformations must be accompanied by a change in hydrogen composition. The need for a composition change creates

some uncertainty in their analyses to determine the habit planes of the product  $\gamma$ -hydride precipitates (and  $\epsilon$ -hydride precipitates) of these transformations as it is not clear if the composition change occurs before, during or after the transformation. In recent years, contradictory statements have emerged concerning the stability of the  $\gamma$ -phase and possible phase transitions between the  $\delta$ - and  $\gamma$ -phases: for example, Steuwer and coworkers (Steuwer et al., 2009) suggested, based on X-ray diffraction observation, that a  $\delta \rightarrow \gamma$  stress-induced martensitic transformation occurs via ordering of the hydrogen atoms, akin to a Snoek-type relaxation, while the conventional view is that if the metastable  $\gamma$ -hydride phase forms at all, it transforms into the stable  $\delta$  phase, i.e.  $\gamma \rightarrow \delta$  (Northwood and Kosasih, 1983; Lanzani and Ruch, 2004). Some of these controversies may be ascribed to the fact that conventional laboratory-based techniques used in the study of these hydride phases are essentially surface techniques. They provide very little information about the micromechanical properties of the hydrides, their crystallography and their relationship with the matrix in the bulk (Une et al., 2004), where additional constraints are likely to change any transformation properties compared to those occurring at the surface. As pointed out by Lanzani and Ruch (Lanzani and Ruch, 2004), the elusive metastable  $\gamma$ -phase is observed mostly after rapid quenching of the Zr alloy sample (e.g.,  $>10 \text{ K min}^{-1}$ ) (Ells, 1968), but eventually transforms into the  $\delta$ -phase at temperatures in excess of  $150 \text{ }^\circ\text{C}$  (Nath et al., 1973). Based on their experimental results, as well as on previous experiments, these authors also concluded that  $\gamma$  is indeed metastable in typical nuclear-grade zirconium alloys such as Zircalloys, while it might be stable in higher purity zirconium ( $>98\text{-}99\%$ ), as proposed earlier by Beck (Beck, 1962) and Mishra and co-workers (Mishra et al., 1972).

Indeed, recent experimental investigations of Zircaloy-4 showed that only the  $\delta$  hydride phase is present in this material over a large range of temperature and hydrogen loading relevant to nuclear application (see, e.g., Kumar et al., 2010; Santisteban et al., 2010). Since the purpose of the present research is to investigate nuclear-grade zirconium alloys, this study can be limited only to the study of the formation, evolution and properties of the stable  $\delta$ -phase within the  $\alpha$ -Zr matrix.

Numerous studies have suggested that the hydride phases grow into grains along particular habit planes of the  $\alpha$ -Zr matrix and various habit planes have been proposed: the prism plane of  $\{10\bar{1}0\}$  (Liu et al., 2008), the pyramidal plane of  $\{10\bar{1}1\}$  (Une and Ishimoto, 2009), the basal plane (0001),  $\{10\bar{1}7\}$ , (Westlake, 1968; Roy and Jacques, 1969) and twinning planes of  $\{10\bar{1}2\}$ ,  $\{11\bar{2}1\}$  and  $\{11\bar{2}2\}$  (Kunz and Bibb, 1960) of the hcp  $\alpha$ -Zr matrix. However the most commonly reported orientation relationship between matrix and precipitate has been (0001)  $\alpha$ -Zr// $(111) \delta$ -ZrH<sub>1.5</sub> orientation relationship (Ells, 1968; Perovic et al 1983). Recently, EBSD characterization of textured Zircaloy-4 sheets showed that the hydrides and the matrix have the (0001)  $\alpha$ -Zr// $(111) \delta$ -ZrH<sub>1.5</sub> orientation relationship at all locations sampled (Kumar et al., 2010).

This orientation relationship was introduced in the model by first assigning each grain an orientation as described in section 1.1 on microstructure generation. Once the basal pole direction of the grain is known, the (111)  $\delta$ -ZrH<sub>1.5</sub> is assigned to be perpendicular to the pole and thus parallel to the basal plane. Within each basal plane, the hydrides will grow in three directions with needles parallel to  $\langle 11\bar{2}0 \rangle$  (Bradbrook, 1972). These directions, at  $120^\circ$  to each other, are selected at random with each plane. Thus, a precipitate that nucleates will have an energetic penalty to grow in any other direction. This condition is introduced by modifying Eq. 12 to

$$P = \exp\left(-\frac{\Delta E + E_p}{k_B T}\right) \quad \text{for} \quad \Delta E + E_p > 0$$

$$P = 1 \quad \text{for} \quad \Delta E + E_p \leq 0$$

Eq. 13

where  $E_p$  is the energy cost for a hydride precipitate to grow in any other direction than the three favored directions. While it is not yet clear if the growth of the  $\delta$ -ZrH<sub>1.5</sub> precipitations in these favored directions is thermodynamically driven to lower its overall energy or kinetically driven by fast growth in that

particular direction, for the purposes of this demonstration the former is chosen. The simulated growth of hydride precipitates in a single crystal of  $\alpha$ -Zr is shown in Figure 14. This simulation was performed with the growth of precipitates being energetically favored in preferred directions in the basal plane. If kinetically-driven growth mechanisms are found to be the cause of the needle shapes, then the model can be easily modified by introducing a growth rate term  $G$  as

$$P = G(\omega) \exp\left(-\frac{\Delta E}{k_B T}\right) \quad \text{for} \quad \Delta E > 0$$
$$G(\omega)P = 1 \quad \text{for} \quad \Delta E \leq 0$$

Eq. 14

where  $G$  is a function of the in-basal direction  $\omega$  of the matrix grain with high growth rate in the favored direction.

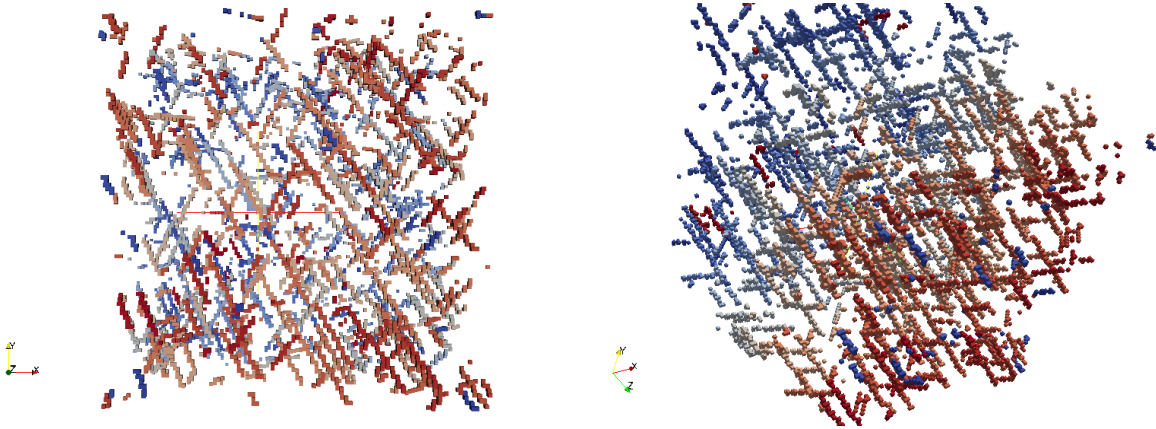


Figure 14. Growth of hydride precipitates in a single crystal of  $\alpha$ -Zr. The same precipitates are shown from two different directions.

## 2.0 SIMULATION OF HYDRIDE PRECIPITATION

The objective is to simulate the precipitation of hydrides following the drying cycle. Following the drying cycle the temperature immediately drops and then decays very slowly over many months and years. Hansen estimated the temperature profile of a fueled cladding by analyzing the heat conduction in a two-dimensional cylinder (Hansen, 2012). He assumed the drying temperature was 400 °C. The temperature profile he obtained is shown in Figure 15, a plot of the cladding temperature starting from the end of the drying cycle when dry storage begins. As one can see as soon as the drying cycle is terminated, the temperature drops very quickly to approximately 320 °C and then gradually decays over a period of years. For demonstration purposes, we simulate this condition by starting the simulation at 400 °C, and drop the temperature immediately to 300 °C. At this point, the zirconium matrix is supersaturated with hydrogen. The temperature is held constant at 300 °C while the hydrides precipitate. A variety of microstructures for the underlying cladding were used. The composition was over-saturated with all the hydrogen dissolved to mimic the drying cycle. The sample temperature is then reduced to 300 °C and held here to simulate precipitation. Nucleation of precipitates could occur at random in any part of grains. Growth of these nucleated precipitates is controlled by the diffusion of hydrogen to the precipitates.

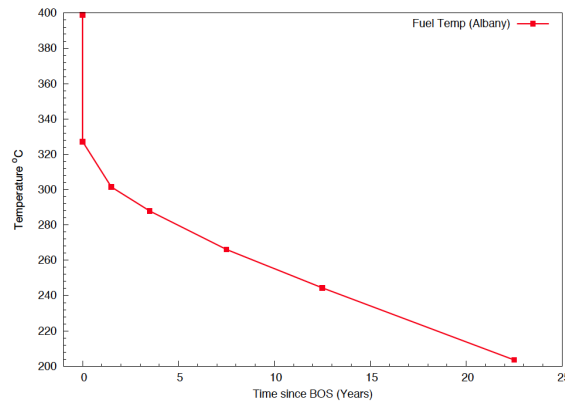


Figure 15. Estimated cladding temperature after drying during dry-storage (Hansen, 2012).

The first set of simulations used a polycrystalline microstructure generated by normal grain growth, thus the grain structure is topologically correct, but is equiaxed as would be expected for normal grain growth. The grains are randomly oriented, but the precipitates within each grain are oriented in the basal plane along the preferred growth directions. This version of the simulation used the simpler definition of the variational derivative of the free energy,

$$\frac{\delta E}{\delta C} = \frac{dE_v}{dC} + \kappa \nabla^2 C \quad \text{Eq. 15}$$

with quadratic fitting of the free energy curves in Figure 13. Two separate simulations were performed from the same underlying cladding microstructure (shown in Figure 16), one with no stress applied and a second with uni-axial stress applied. Since the model is not yet coupled to a mechanics model, the stress applied was a simple, constant uni-axial tensile stress that did not change with the nucleation and growth of precipitates.

The hydride precipitates that grow in this grain structure are shown in Figure 17. Within each grain, the precipitates are aligned with each other along their preferred growth directions, however, the different grains are oriented differently and therefore the precipitates in the overall structure have many different orientations.

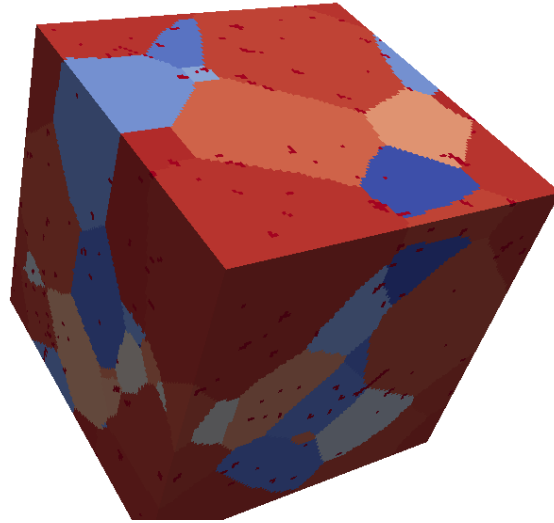


Figure 16. Starting microstructure for the hydride precipitation simulations.

The stress was introduced in the simulation by adding a strain energy term  $E_s$  to the free energy. The strain energy of the precipitate was related to the direction of applied stress as

$$E_s = \varepsilon \sin(\phi - 45) \quad \text{Eq. 16}$$

where  $\varepsilon$  is a constant and is a function of the applied stress and strain accompanying hydride nucleation or growth and  $\phi$  is the misorientation angle between the direction of the applied stress and precipitate growth direction. Note in this method of calculation, precipitates that are perpendicular to the applied stress direction have an energetic advantage to nucleate and grow; while those parallel to the applied stress have an energetic penalty and those at  $45^\circ$  are not affected by the applied stress. By careful examination of Figures 17 and 18, it can be seen that there are some precipitates that are oriented vertically in Figure 17, with no applied stress; while there are no precipitates that are oriented vertically in Figure 18 with an applied tensile stress in the vertical direction. Furthermore, there are more precipitates that are oriented more than  $45^\circ$  from the applied stress direction and these appear to be longer. This is supported by an analysis of precipitate size distribution of the two cases of applied stress and no stress, shown in Figure 19. The same data are plotted on a log scale for the number of precipitates of a given size. The linear plot shows that in the case where there is no stress in the cladding sample, many small precipitates are present. The log plot shows that the cladding with uniaxial stress applied consistently has more precipitates that are larger. It is clear why a larger number, but smaller precipitates formed when no stress was applied in the simulations; since a smaller number of precipitates that are favorably oriented nucleate and grow, the hydrogen diffuses preferentially to these sites allowing them to grow larger. A review of the literature did support the biased orientation of the precipitates as expected; however, no experimental evidence was found to support the observation that the precipitates may be larger when perpendicular to the applied stress. This may be due to the fact that this aspect of precipitate growth has not been examined experimentally or it may be that other factors such as the compressive stress field that, without doubt, forms around the precipitates may limit their growth under any stress condition. A more evolved model that can couple the local micro-stresses may be able to answer these questions.

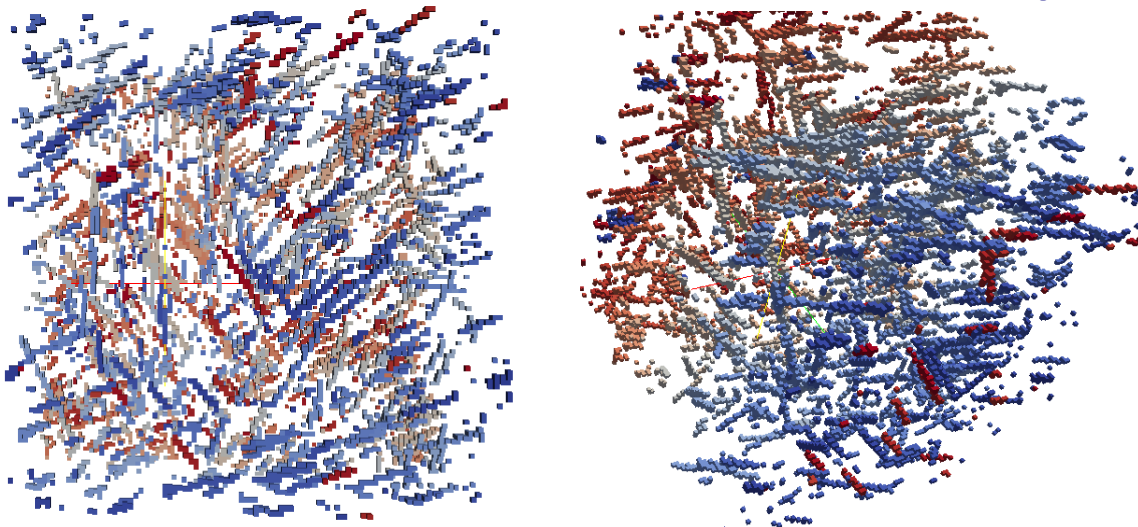


Figure 17. All in the precipitates in the polycrystalline are imaged and shown from two different angles.

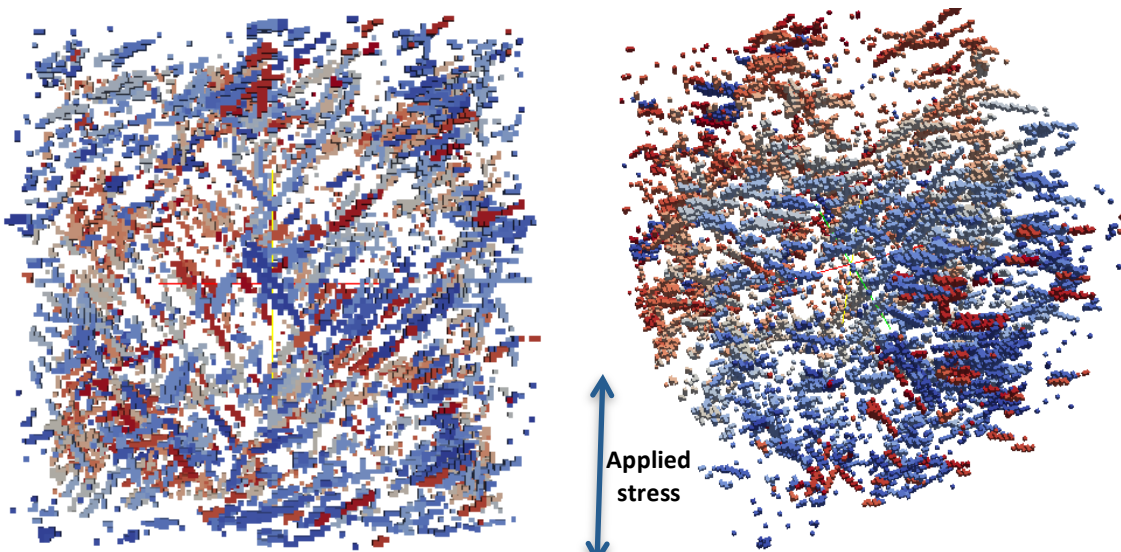


Figure 18. The same simulation was run with a uni-axial, constant stress applied.

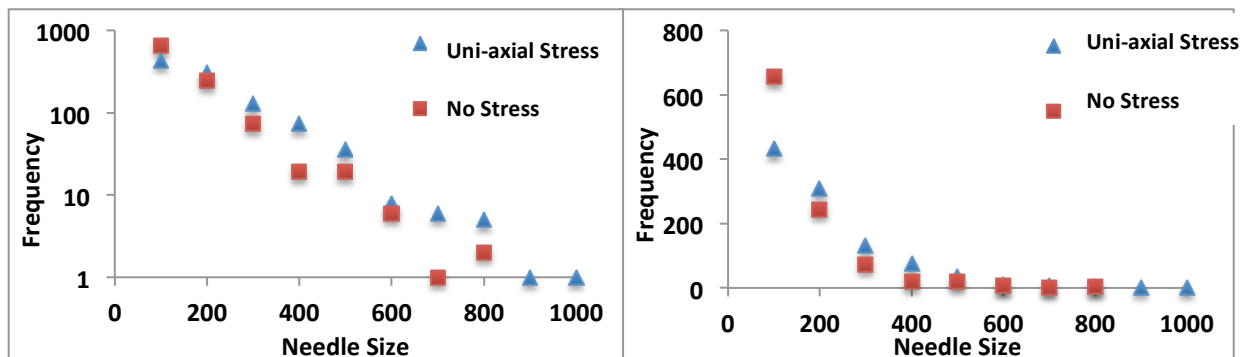


Figure 19. Precipitation size distribution in a polycrystalline Zr-matrix with randomly oriented grains for the case of no applied stress and application of a constant, uni-axial stress. The same data are shown on a log- and normal-plots. The log plot shows the data more clearly for larger needle sizes and the linear plot shows the data more clearly for the smaller shorter needles.

A second set of simulations used the rolled microstructures generated as described in section 1.1. In these simulations the grains had an average elongation of 2x in the rolling direction as compared to the transverse and normal directions and the  $\alpha$ -Zr grains were oriented with preferred orientation of the basal poles with frequency given by Eq. 1 and Figure 7. The starting composition was over-saturated with all the hydrogen dissolved in the  $\alpha$ -Zr matrix at a temperature of 400 °C, then the temperature was reduced to 300 °C and held constant during the simulation. The results of this simulation are presented in this section. Relatively small simulations with limited number of grains were performed to demonstrate model capability. The microstructure generated using Dearm3D, shown in Figure 20, has elongated grains in one direction and not in the others. This orientation is selected for illustration purposes.

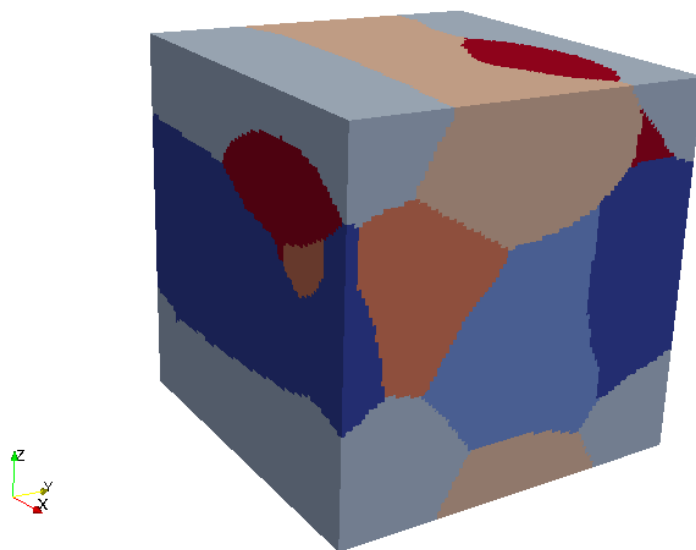


Figure 20. Input microstructure with basal orientation stochastically assigned using Eq. 1 for small simulations with seven grains. The grains are elongated in the X-direction, which is also the rolling direction for the purposes of this illustration.

Two simulations using this rolled starting microstructure are shown here. In one, the nucleation sites are predominantly near the grain boundary as observed experimentally (Ells 1968, Bradbrook 1972, Qin et al., 2011). In the other simulation, the nucleation sites for precipitates can occur with equal probability anywhere in the grain structure; in other words, nucleation sites such as dislocation loops are evenly distributed. The nucleation and growth of precipitates with preferred nucleation sites at grain boundaries is shown in Figure 21. The same microstructures are shown from two different angles, an oblique angle and one along the rolling direction of the cladding. In the early stages, nucleation and growth occur concurrently, that is to say as nuclei are forming they start to grow immediately, while other nuclei continue to form. In the intermediate stages, nucleation decreases and the growth of the precipitates dominates. At the end, the existing nuclei continue to grow with virtually no new nuclei forming until hydrogen in the matrix is depleted to its solubility limit. The view shown in Figure 21 d, e and f, looking down the rolling direction roughly orthogonal to the grain boundaries, clearly shows that precipitates are nucleating and growing primarily near grain boundaries. While it is not clear from these pictures, precipitates do not cross grain boundaries as the crystallographic direction changes in the neighboring grains. This is consistent with the fact that precipitates grow along particular crystallographically favored directions. The growth of precipitates in this demonstration is controlled by diffusion of hydrogen to the precipitates. Diffusion-limited kinetics in this model has been investigated for simple geometries in previous work (Homer et al., 2013; Tikare and Schultz, 2012) and shown to be simulated correctly.

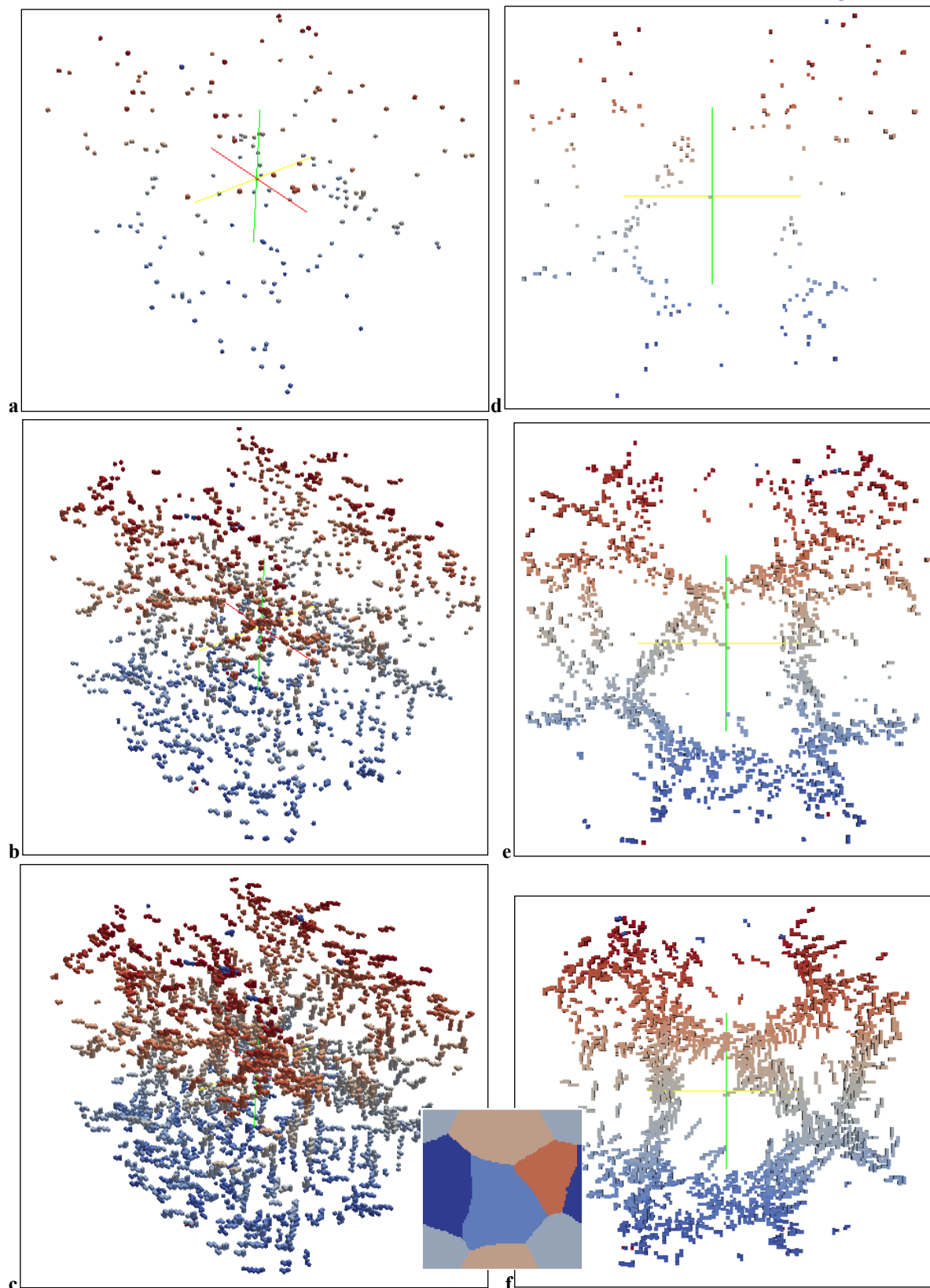


Figure 21. a, b, and c. Nucleation and growth of  $\delta$ -ZrH<sub>1.5</sub> precipitates at time = 3, 27 and 520 Monte Carlo Steps (MCS). Nucleation sites are predominantly at grain boundaries, which is very clearly illustrated in

d, e and f, where the same precipitates seen in a, b and c are imaged, but now looking down the rolling direction. The inset between c and f is provided to show the grain boundaries at the surface of the sample and is the same microstructure shown in Figure 20.

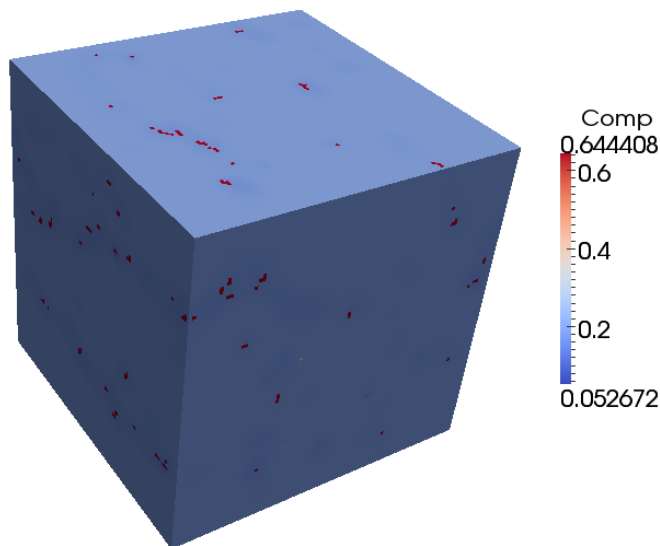


Figure 22. The distribution of hydrogen in the microstructure; hydrogen concentrations are highest in the  $\delta$ -ZrH<sub>1.5</sub> precipitates and the matrix is depleted.

Since, we assume that the kinetics of precipitation growth is controlled by hydrogen diffusion from the matrix to the precipitate, the distribution of hydrogen in the matrix should be highest in regions away from the precipitate, decrease as the precipitate surface is approached and then increase sharply at the precipitate surface. This distribution is clearly shown in Figure 22, the distribution of hydrogen in the rolled microstructure corresponding to precipitates in Figure 21 c. The hydrogen concentration is highest in the precipitates and corresponds to a stoichiometry of ZrH<sub>1.6</sub>, which is very close to that observed experimentally. The hydrogen content in the matrix is depleted with the highest depletion close to the precipitate surface and increases in the matrix away from precipitates. This is expected in diffusion-controlled phase changes such as in the one being simulated here. In order to show the hydrogen distribution more clearly, the hydrogen distribution in a 2D slice through the cladding shown in Figures 21 & 22 is shown in Figure 23, grain structure with precipitates is shown in Figure 23a, with the corresponding hydrogen distribution in Figure 23b. The red features are the precipitates in the microstructure in Figure 23a and the high hydrogen content of the hydrides in Figure 23b. The composition distribution shows high H-content in the precipitates, as expected, with a sharp decrease in hydrogen in the matrix immediately surrounding the precipitate and a gradual increase in regions away from the precipitate. Since this is a 2D slice through the 3D microstructure, the region with depleted hydrogen away from precipitates in the slice are near precipitates either above or below the slice that is imaged here. It is worth noting that in these simulations diffusion-controlled kinetics is assumed for the purpose of demonstrating the model; however, should interfacial-reaction be identified later as the limiting process for precipitate growth, the code for this process has already been written and verified.

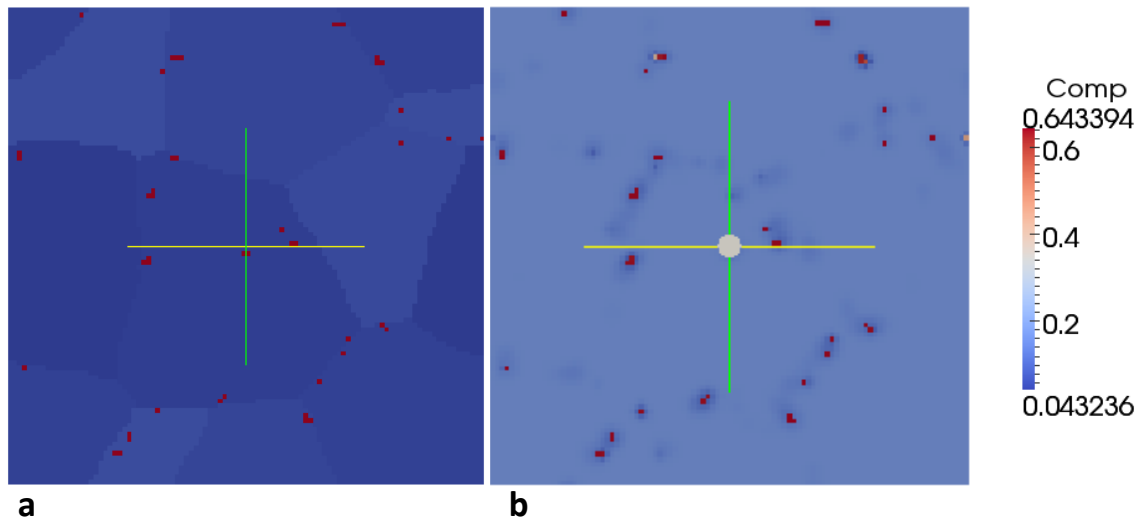


Figure 23. A slice through the microstructure shown in Figures 21 & 22. In a, the grain structure shown in blue with red precipitates and, in b, the composition corresponding to this slice. The red in b are regions of high hydrogen content, which is where the precipitates are located.

The simulation showing nucleation of hydride precipitates randomly distributed in the microstructure with equal probability of occurring anywhere is shown in Figure 24. Again, a similar trend is seen. At first nucleation events predominate and as these first nuclei grow, others precipitates continue to nucleate at a slower rate and finally growth of existing precipitates dominates. The hydrogen distribution in the microstructure is consistent with diffusion-controlled precipitate growth as shown in Figure 25. As noted before, precipitates do not cross grain boundaries as the crystallographic orientations in adjacent grains change. While the overall hydride precipitation behavior is similar between the two cases, the precipitates grow more quickly in the spatially randomly-nucleating precipitates as shown in Figure 26, a comparison of total precipitate formation for the two cases considered. The precipitate formation growth for the randomly distributed nuclei is faster than for the precipitates that nucleate near the grain boundaries. This difference in behavior is explained by the diffusion distance for hydrogen. As the precipitates cluster near the grain boundaries, the diffusion distance for hydrogen from the grain centers to the precipitates becomes longer, thus increasing diffusion times and reducing the rate of precipitate nucleation and growth. Again, this is consistent with diffusion-controlled precipitate growth kinetics.

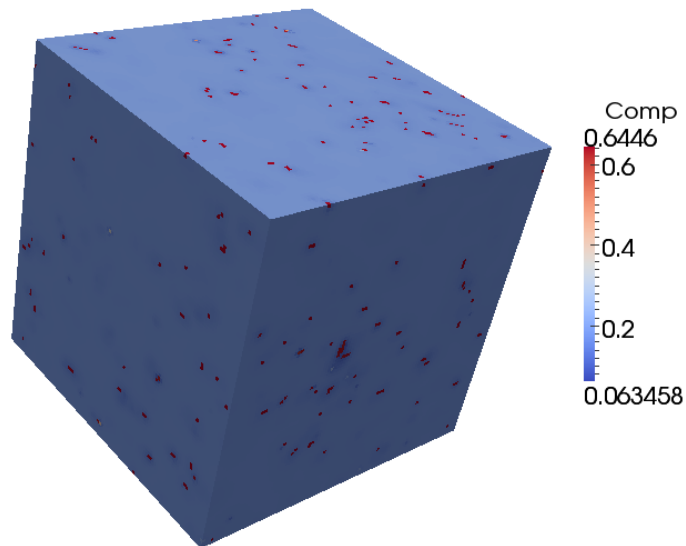
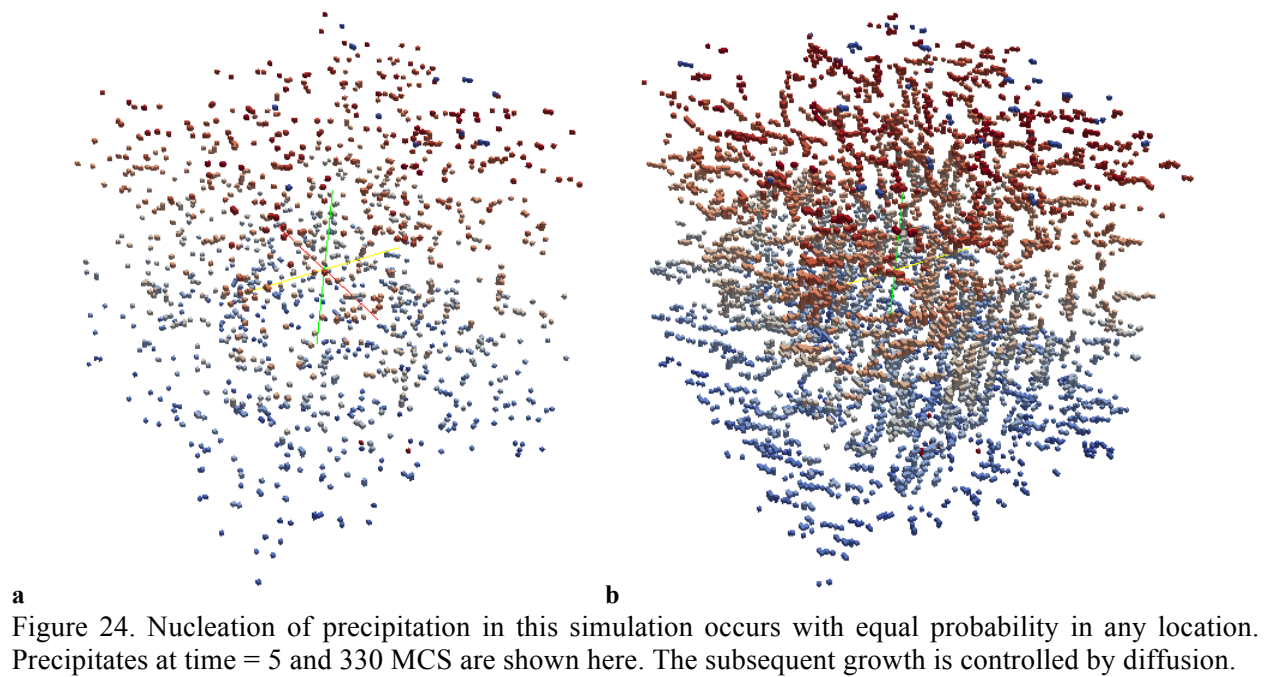


Figure 25. The distribution of hydrogen in the microstructure for the simulation results shown in Figure 24.

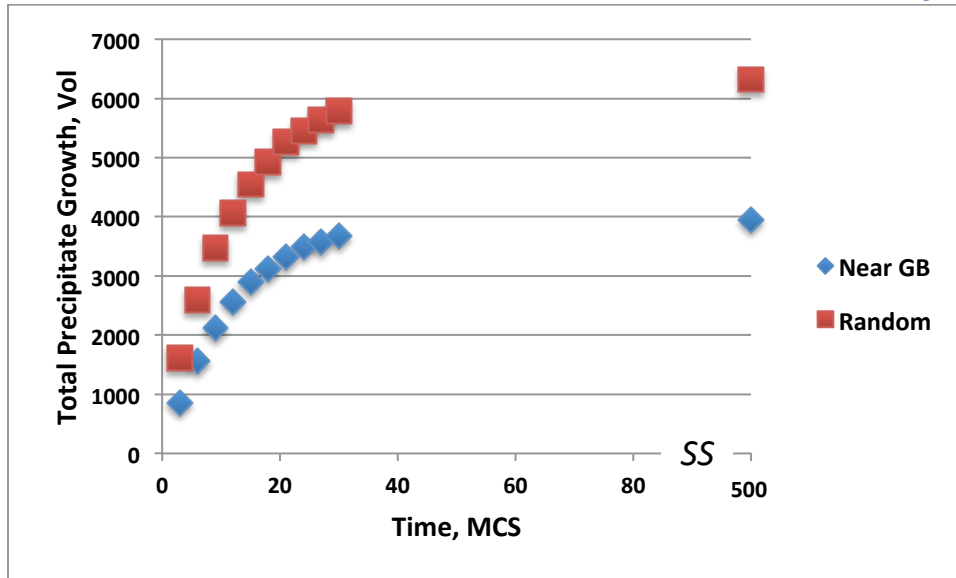


Figure 26. A comparison of total precipitate formation for the two cases where nucleation occurs randomly with uniform probability anywhere in the grains and nucleation occurs preferentially at the grain boundaries.

### **3.0 SUMMARY AND CONCLUSIONS**

The precipitation of  $\delta$ -ZrH<sub>1.5</sub> in  $\alpha$ -Zr matrix by nucleation and growth in a Zircaloy-4 microstructure has been demonstrated. All the basic microstructural evolution processes necessary to simulate hydride precipitation were incorporated into the model and demonstrated. The results of the model show good qualitative agreement with experimental observations. The underlying microstructures of Zr-based claddings can be computationally generated to match the available experimental data on the specific systems; this capability was demonstrated on rolled Zircaloy-4 microstructure with geometric elongation and crystallographic orientation to match the data available about these features. The thermodynamic free energies were obtained using CALPHAD-type calculations for  $\alpha$ -Zr,  $\delta$ -ZrH<sub>1.5</sub>,  $\gamma$ -ZrH and  $\epsilon$ -ZrH<sub>2</sub> phases. The calculated free energies for  $\alpha$ -Zr and  $\delta$ -ZrH<sub>1.5</sub> phases were used for the hydride precipitate formation simulations. At the present time, the other two hydride phases,  $\gamma$ -ZrH and  $\epsilon$ -ZrH<sub>2</sub>, were not considered in the precipitation simulations, since a review of experimental data indicated that these do not contribute to hydride formation in the claddings during dry storage conditions. The model uses the full chemical potential of the two phases with both components in preparation for the more complex compositions that will be simulated in the near future. The phase transformation from  $\alpha$ -Zr to  $\delta$ -ZrH<sub>1.5</sub> leading to precipitation by nucleation and growth of precipitates can be simulated. The nucleation rate and subsequent growth of the precipitates is controlled by diffusion of hydrogen. The growth of the precipitates occurred in energetically favorable crystallographic directions. While it is not clear that the growth occurs in particular directions due to thermodynamics of the precipitate growth, this method was chosen for demonstration. However, should the kinetics of precipitate growth prove to be the controlling factor that determines the precipitate growth, the model can be modified to simulate the kinetic mechanism. The nucleation sites of the precipitates, dislocation loops or other defects, can be distributed to match those in the actual materials. We have demonstrated this by allowing nucleation to occur with equal probability anywhere in the grains or predominantly near grain boundaries. Lastly, the effect of applied stress on orienting the precipitate growth was demonstrated. While a very simple, constant, uniaxial stress was used to simulate the preferred growth, it is sufficient to demonstrate the model capabilities. A true micro-mechanical model that can calculate the local complex stress resulting from precipitate growth will be incorporated in the near future.

The next steps to further develop the model will address several issues that are briefly addressed here. To enable validation, all the parameters and results will be quantified, so a more rigorous comparison to known results can be conducted and the simulation results can be more predictive. The model has been verified extensively to show that it does simulate diffusion-controlled precipitate growth with the crystallographic orienting behavior observed. However, validation by direct comparison to experimental data has been limited. We will identify validation exercises to ensure that predictive capability is developed. We will identify cladding materials characteristics that influence hydride precipitate formation behavior the most. These may be the role of second phase particles and additional chemical components. If these materials characteristics prove to be significant, they will be incorporated into the model. The micro-mechanics of precipitate nucleation and growth will also be incorporated. Finally, constitutive models for use in continuum, engineering-scale model of cladding performance will also be developed.

## **REFERENCES**

- Abe, H. & Furugen, M. (2010) Method of Evaluating Workability in Cold Pilgering of Zirconium Alloy Tube Materials Transactions, 51, 1200-1205.
- Barracough, K.G., & Beevers, C.J. (1970) Some Observations of the Phase Transformations in Zirconium Hydrides. *Journal of Nuclear Materials*, 34, 125-134.
- Bashkin, I.O., Malyshev, V. Yu., & Myshlyaev, M.M. (1992) Reversible  $\gamma \rightarrow \alpha + \delta$  transformation in zirconium deuteride. *Soviet Physics Solid State*, 34, 1182-1184.
- Beck, R.L. (1962) Zirconium-Hydrogen Phase System. *Transactions ASM*, 55, 542-555.
- Birk, S., Hanson, B., Marschman, S., Sindelar, B., Sorenson, K., & Wagner, J. (2012) Used Nuclear Fuel Storage and Transportation Research, Development and Demonstration Plan, *FCRD-FCT-2012-000053*.
- Blomquist, J., Oloffson, J., Alvarevol, A.-M., & Bjerken, C. (2010) Structure and Thermodynamic Properties of Zirconium Hydrides from First Principles. Preprint, University of Malme, Sweden.
- Bradbrook, J.S., Lorimer, G.W., & Ridley, N. (1972) The Precipitation of Zirconium Hydride in Zirconium and Zircaloy-2 *Journal of Nuclear Materials*, 42, 142-160.
- Cassidy, M.P., & Wayman, C.M. (1980) The Crystallography of Hydride Formation in Zirconium: I. The  $\delta \rightarrow \gamma$  Transformation. *Metall. Trans. A*, 11A, 47-56.
- Cassidy, M.P., & Wayman, C.M. (1980) The Crystallography of Hydride Formation in Zirconium: II. The  $\delta \rightarrow \epsilon$  Transformation. *Metall. Trans. A*, 11A, 57-67.
- Coleman, C.E., Grigoriev, V., Inozemtsev, V., Markelov, V., Roth, M., Makarevicius, V., Kim, Y.S., Ali, K.L., Chakravarthy, J.K., Mizrahi, R., & Lalgudi, R. (2010) *J. ASTM Int.*, 7 (5).
- Colas, K.B, Mott, A.T. Almer, J.D., Daymond, M.R., Kerr, M., Banckik, A.D., Vizcaino, P., Santisteban, J.R. (2010) In situ study of hydride precipitation kinetics and re-orientation in Zircaloy using synchrotron radiation, *Acta Materialia* 58 6575-6583
- Danielson, P.E, & Sutherlin, R.C. (2004) Metallography and Microstructures of Zirconium, Hafnium, and Their Alloys, *Metallography and Microstructures, ASM Handbook, ASM International*, 9, 942-958
- Ells, C.E. (1968). Hydride Precipitates in Zirconium Alloys (A Review). *Journal of Nuclear Materials*, 28, 129-151.
- Fong, R.W.L. (2013) Anisotropy factors from texture and mechanical strain in Zircaloy-4 fuel sheaths. *Journal of Nuclear Materials*, 440, 288-297.
- Glazoff, M.V. Modeling of Some Physical Properties of Zirconium Alloys for Nuclear Applications in Support of UFD Campaign, *IN/EXT-13-29581*.
- Hansen, G. (2012) 2D Multimaterial Heat Conduction in Cylindrical Geometry With Source, unpublished work
- Hanson, B., Alsaed, H., Stockman, C., Enos, D., Meyer, R., and Sorenson, K. (2011) Gap Analysis to Support Extended Storage of Used Nuclear Fuel, *FCRD-USED-2011 000136, PNNL-20509*.
- Hill, R. (1948) A theory of the yielding and plastic flow of anisotropic metals. *Proc. Roy. Soc. A, London*, 193, 281-297.
- Homer, E.R, Tikare, V. and Holm, E.A. (2013) Hybrid Potts-Phase Field Model for Coupled Microstructural-Compositional Evolution, *Comp. Mater. Sci.*, 69 414-423.

- Hunt, C.E.L. (1975) Anisotropic theory and the measurement and use of the anisotropic factors for Zircaloy-4 fuel sheaths, in *Transactions, 3rd Int. Conf. on Structural Mechanics in Reactor Technology*, London, UK, vol. 1, Paper C 2/9.
- Jackson, M.A. (2013) Digital Representation Environment for Analyzing Microstructure in 3D, <http://dream3d.bluequartz.net/>
- Kearns, J.J., & Woods, C.R. (1966) Effect of Texture, Grain Size, and Cold Work on the Precipitation of Oriented Hydrides in Zircaloy Tubing and Plate. *Journal of Nuclear Materials*, 20, 241-261.
- Kearns, J.J. (1967) Terminal Solubility and Partitioning of Hydrogen in the Alpha Phase of Zirconium, Zircaloy-2 and Zircaloy-4, *Journal of Nuclear Materials*, 22, 292-303
- Kiran Kumar, N.A.P., Szpunar, J.A., & He, Z. (2010) Preferential Precipitation of Hydrides in Textured Zircaloy-4 Sheets. *Journal of Nuclear Materials*, 403, 101-107.
- Kolesnikov, A.I., Balagurov, A.M., Bashkin, I.O., et al. (1994) Neutron Scattering Studies of Ordered  $\gamma$  - ZrD. *J. Phys: Condensed Matter*, 6, 8977-8988.
- Kunz, F.W., & Bibb, A.E. (1960) Habit Plane of Hydride Precipitation in Zirconium and Zirconium-Uranium. *Transactions of the American Institute of Mining and Metallurgical Engineers*, 218, 133-135.
- Lanzani, L., & Ruch, M. (2004) Comments on the Stability of Zirconium Hydride Phases in Zircaloy. *Journal of Nuclear Materials*, 324, 165-176.
- Liu, Y.Z., Peng, Q., Zhao, W.J., & Jiang, H.M. (2008) Hydride Precipitation by Cathodic Hydrogen Charging Method in Zirconium Alloys. *Materials Chemistry and Physics*, 110, 56-60.
- Louthan Jr., M.R., & Marshall, R.P. (1963) Control of Hydride Orientation in Zircaloy. *Journal of Nuclear Materials*, 9, 170-184.
- Marshall, R.P. (1967) Control of Hydride Orientation in Zircaloy by Fabrication Practice. *Journal of Nuclear Materials*, 24, 49-59.
- Mishra, S., Sivaramakrishnan, K.S., & Asundi, M.K. (1972) Formation of the Gamma Phase by a Peritectoid Reaction in the Zirconium-Hydrogen System. *Journal of Nuclear Materials*, 45, 235-244.
- Motta, A.T., & Chen, L.-Q. (2012) Hydride Formation in Zirconium Alloys. *JOM*, 64, 1403-1408.
- Nath, B., Lormier, G.W., & Ridley, N. (1973) Relationship Between Gamma-Hydrides and Delta-Hydrides in Zirconium-Hydrogen Alloys of Low Hydrogen Concentration. *Journal of Nuclear Materials*, 49, 262-280.
- Northwood, D.O., & Kosasih, U. (1983) Hydrides and Delayed Hydrogen Cracking in Zirconium and its Alloys. *International Metals Review*, 28, 92.
- NUREG / CR-7116, (2011) Materials Aging Issues and Aging Management for Extended Storage and Transportation of Spent Nuclear Fuel.
- Ostberg, G. (1962) Determination of Hydride Solubility in Alpha Phase Zirconium, Zircaloy-2, and Zircaloy-4, *Journal of Nuclear Materials*, 5, 208-215.
- Payne, M.C., Teter M.P., Allan D.C., Arias T.A., Joannopoulos, J.D. (1992) Iterative minimization techniques for ab initio total-energy calculations: molecular dynamics and conjugate gradients, *Rev. Mod. Phys.*, vol. 64, 1045-1097 92.
- Perovic, V., Weatherly, G.C. & Simpson C.J. (1983) Hydride Precipitation in  $\alpha/\beta$  Zirconium Alloys, *Acta Metallurgica*. 3, 1381-1391.

Plimpton S., Battaile C., Chandross M., Holm L., Thompson A., Tikare V., Wagner G., Webb, E., Zhou, X., Garcia Cardona, C., Slepoy A., (2009) Crossing the Mesoscale No-Man's Land via Parallel Kinetic Monte Carlo Sandia report SAND2009-6226

Puls, M.P. (2012) The Effect of Hydrogen and Hydrides on the Integrity of Zirconium Alloy Compounds Delayed Hydride Cracking. Springer.

Qin, W., Kiran Kumar, N.A.P., Szpunar, J.A. & Kosinski, J. (2011) Intergranular  $\delta$ -hydride nucleation and orientation in zirconium alloys, *Acta Materialia*, 59, 7010-7021.

Roy, C., & Jacques, J.G. (1969) (1017) Hydride Habit Planes in Single Crystal Zirconium. *Journal of Nuclear Materials*, 31, 233-237.

Santisteban, J.R., Vicente-Alvarez, M.A., Vizcaíno, P., Banchik, A.D., & Almer, J.D. (2010) Hydride Precipitation and Stresses in Zircaloy-4 Observed by Synchrotron X-Ray Diffraction. *Acta Materialia*, 58, 6609-6618.

Santisteban, J.R., Vicente-Alvarez, M.A., Vizcaino, P., Banchik, A.D., Vogel, S.C., Tremsin, A.S., Vallergera, J.V., McPhate, J.B., Lehmann, E., & Kockelmann, W. (2012) Texture imaging of zirconium based components by total neutron cross-section experiments. *Journal of Nuclear Materials*, 425, 218-227.

Sidhu, S.S., Murthy, N.S.S., Campos, F.P., & Zaubers, D.D. (1963) Neutron and X-Ray Diffraction Studies of Nonstoichiometric Metal Hydrides. *Advances in Chemistry Series*, 39, 87-98.

Tikare, V. and Homer E.R. (2012) Hybrid Potts-Phase Field Model Development and Application *FCT NEAM FMM Report MS-12SN060613*.

Tikare, V. and Schultz P.V. (2012) Verification and Validation of the Hybrid Potts-Phase Field Model for Coupled Microstructural-Compositional Evolution, *FCT NEAMS VVUQ Report M3MS-12SN060602*.

Une, K., Nogita, K., Ishimoto, S., & Ogata, K. (2004) Crystallography of Zirconium Hydrides in Recrystallized Zircaloy-2 Fuel Cladding by Electron Backscatter Diffraction. *Journal of Nuclear Science and Technology*, 41, 731-740.

Une, K., & Ishimoto, S. (2009) Crystallographic Measurement of the Beta to Alpha Phase Transformation and Delta-Hydride Precipitation in a Laser-Welded Zircaloy-2 Tube by Electron Backscattering Diffraction. *Journal of Nuclear Materials*, 389, 436-442.

Wang, Z., Garbe, U., Li, H., Harrison, R. P., Toppler, K., Studer, A. J., Palmer, T., & Planchenault, G. (2013) Hydride precipitation and its influence on mechanical properties of notched and unnotched Zircaloy-4 plates. *Journal of Nuclear Materials*, 436, 84-92.

Westlake, D.G. (1968) Habit Planes of Zirconium Hydride in Zirconium and Zircaloy. *Journal of Nuclear Materials*, 26, 208-216.

Yamanaka, S., Miyake, M., & Katsura, M. (1997) Study on the Hydrogen Solubility in Zirconium Alloys, *Journal of Nuclear Materials*, 247, 315-321. Zhao, Z., Morniroli, J.-P., Legris, A., Ambard, A., Khin, Y., Legras, L., & Blat-Yrieix, M. (2008). Identification and Characterization of a New Zirconium Hydride. *Journal of Microscopy*, 232, 410-421.

Zuzek, E, Abriata, J.P., San-Martin, A., & Manchester, F.D. (1990) In: Massalski, T.B., editor. H-Zr (Hydrogen-Zirconium), Binary Alloy Phase Diagrams, II Ed. vol. 2, p 2078-2080.

Zuzek, E, Abriata, J.P., San-Martin, A., & Manchester, F.D. (2000) In: Manchester, F.D., editor. Phase diagrams of binary hydrogen alloys. Materials Park, OH, ASM International, p. 309.